Spin dynamics of chromium. II. Incommensurate alloys

R. S. Fishman
*Solid State Division, Oak Ridge National Lab, Oak Ridge, Tennessee 37831-6032**
and Department of Physics, North Dakota State University, Fargo, North Dakota 58105-5566

S. H. Liu
Department of Physics, University of California, San Diego, California 92093
(Received 26 January 1996; revised manuscript received 1 May 1996)

Since the magnetic moments of transition-metal antiferromagnets are created by electron-hole pairs, the spin dynamics of Cr alloys are associated with quasiparticle transitions. In this paper, we use the random-phase approximation to investigate the spin dynamics about the two different spin-density-wave (SDW) states of incommensurate (I) alloys with wave vectors $\mathbf{Q}'_{\pm}=(2\pi/a)(0,0,1\pm\partial')$. Because of their more complex quasiparticle energies, I alloys have a richer spectrum of collective excitations than the commensurate (C) alloys studied in the previous paper. Associated with the free energy's rotational invariance are transverse spin-wave (SW) modes which evolve from each satellite wave vector $\mathbf{Q}'_{\pm}$ with the same temperature-independent mode velocity $c=v_F/\sqrt{3}$ as in the C regime. The translational invariance of the ISDW state is responsible for longitudinal phason modes which evolve from the satellite wave vectors and are damped for any nonzero frequency. As $T\rightarrow T_N$, the phason mode velocity approaches c. Together with a related longitudinal damped excitation, the phason modes tilt the SW cones towards $\mathbf{G}/2=(2\pi/a)$ (0,0,1) and produce a peak in the $\mathbf{G}/2$ cross section at 60 meV, as observed experimentally. High-frequency amplitude modes, both transverse and longitudinal, lie near the pair-breaking edge for each satellite, which is about 40% lower than in the C case. Undamped collective modes called wavons are associated with fluctuations of the SDW wave vectors $\mathbf{Q}'_{\pm}$ about their equilibrium values. Wavon modes were recently observed as peaks in the satellite cross sections between 15 and 20 meV. Our model predicts the temperature and doping dependences of the phason and wavon peaks. [S0163-1829(96)06934-2]

I. INTRODUCTION

Of the known transition-metal antiferromagnets, only Cr alloys have been observed[1] in an incommensurate (I) phase where the wavelength of the spin-density wave (SDW) is not a multiple of the lattice constant. Unlike the single SDW state of commensurate (C) alloys with wave vector $G/2\equiv 2\pi/a$ and period a, the SDW state of I alloys superimposes two different SDW's with wave vectors $\mathbf{Q}'_{\pm}$ on either side of $G/2$. Each ISDW with wave vector $\mathbf{Q}'_{\pm}$ consists of spin-triplet pairs of electrons (a) and holes ($b\pm$) separated by a wave vector $\mathbf{Q}'_{\pm}$. Because the condensate contains an equal number of $ab+$ and $ab-$ electron-hole pairs, I Cr alloys are unique among magnetic and superconducting systems. The coupling between the $ab+$ and $ab-$ condensates is responsible for many of the interesting dynamical properties of I Cr alloys. While much is known experimentally[2–8] about the spin dynamics of I alloys, very little is known theoretically. Most previous theoretical studies[9–12] of the I dynamics relied on a simplistic two-band model only appropriate in the C phase. In this paper, we use the random-phase approximation (RPA) developed in the preceding work[13] (paper I) to study the I spin dynamics of Cr alloys within a three-band model for the a electrons and $b\pm$ holes. This permits a systematic investigation of the longitudinal and transverse excitations about the two SDW states of an I alloy.

The electron and hole Fermi surfaces of Cr alloys are nearly nested by the wave vectors $Q_{\pm}=(G/2)(1\pm\partial)$, which can lie along any of the three crystal axis. For pure Cr, $\partial\approx 0.05$, so that the hole Fermi surface is slightly larger than the electron Fermi surface.[1] In order to minimize the nesting free energy on both sides of the electron and hole Fermi surfaces,[14] the SDW wave vectors $Q'_{\pm}=(G/2)(1\pm\partial')$ are closer to $G/2$ than the nesting wave vectors. The periodicity of the SDW can be controlled by doping Cr with another transition metal. With Mn doping, the electron surface grows, ∂ and ∂' decrease, and the Néel temperature increases. When the Mn concentration exceeds[1] about 0.3%, the CSDW state is stabilized with $\partial'=0$. With V doping, the hole surface grows, ∂ and ∂' increase, and the Néel temperature decreases. Pure Cr and CrV alloys are in an ISDW state with $\partial>\partial'\geqslant 0$. Another useful measure of the commensurability of the SDW is the energy mismatch $z_0=(v_F/\sqrt{3})4\pi\partial/a$, which directly affects the quasiparticle energies.

The three different domains for the SDW wave vectors along any crystal axis correspond to the three possible ways of nesting the electron and hole Fermi surfaces. When an I alloy is cooled in a magnetic field, the SDW wave vectors are aligned parallel to the field direction. Here we study the spin excitations about the two SDW wave vectors along the $\hat{z}$ axis. In units of $2\pi/a$, the SDW wave vectors can then be written as $(0,0,1\pm\partial')$.

As discussed in paper I, the spin dynamics of itinerant antiferromagnets are produced by quasiparticle transitions. Consequently, the spin dynamics sensitively depends on the band structure. The simplest model for the quasiparticle energies of I Cr alloys is the two-band model introduced by

Fedders and Martin.[15] Each ISDW is then independently generated by the Coulomb attraction $U>0$ between electrons and holes separated by $\mathbf{Q}'_{\pm}$. Within the three-band model introduced by Young and Sokoloff,[16] the nesting of the electrons and $b\pm$ holes is directly affected by the mismatch between the electrons and $b\mp$ holes on the same side of the Fermi surface. Hence the self-consistent equation for the SDW order parameter g couples the two ISDW's.

The ''canonical'' free energy is obtained upon integrating this self-consistent equation. Because there is only a single CSDW, the C free energies constructed from the two- and three-band models are identical. But in the I phase, both the self-consistent equation and the free energy are different for the two- and three-band models.[13]

While the first harmonics of the SDW with wave vectors $\mathbf{Q}'_{\pm}$ drive the antiferromagnetic transition, other harmonics have also been observed. The second harmonic of the SDW corresponds to a charge-density wave[17] (CDW) with wave vectors $2\mathbf{Q}'_{\pm}$ on either side of $\mathbf{G}=4\pi\hat{z}/a$. Because it is created by the coupling between the two ISDW's the CDW can only be generated within the three-band model. The third harmonic[18] of the SDW, with wave vectors $3\mathbf{Q}'_{\pm}$, flattens the peaks of the total spin density. Experimentally, the weight of the third harmonic is about 3% of the fundamental for pure Cr, and decreases with V doping. Neither of these higher harmonics are included in the ''canonical'' free energy.

Spin excitations with wavevector $\mathbf{q}$ and frequency ω are associated with quasiparticle transitions between energies $\epsilon(\mathbf{k})$ and $\epsilon'(\mathbf{k}+\mathbf{q})=\epsilon(\mathbf{k})+\omega$. Within the two-band model, each ISDW is generated independently, so quasiparticle transitions about the ISDW at $Q'_{\pm}$ are not affected by the ISDW at $Q'_{\mp}$. Previous predictions[9] for the I dynamics based on the two-band model were inconsistent with many experiments. By contrast, the coupling between ISDW's within the three-band model allows quasiparticle transitions from one ISDW state to the other. We shall show that this dynamical coupling has profound consequences. Unlike the two-band model, the three-band model also permits the formation of a CDW.

Possible transitions among the three I bands of quasiparticles produce a rich spectrum of collective excitations.[19] Each collective mode can be associated with some fluctuation of the SDW. Using the inverse Green's function of Eq. (9) in paper I with arbitrary phases $\phi_{\pm}$ for the two SDW's, and neglecting the spatial extension of the d-band electrons, the equilibrium spin at site $\mathbf{R}$ can be written

$$\begin{aligned}\mathbf{S}_0(\mathbf{R}) &= \mathbf{S}_{0+}(\mathbf{R})+\mathbf{S}_{0-}(\mathbf{R}) \\ &= \alpha_s g\hat{m}\{\cos(\mathbf{Q}'_+\cdot\mathbf{R}+\phi_+)+\cos(\mathbf{Q}'_-\cdot\mathbf{R}+\phi_-)\} \\ &= 2\alpha_s g\hat{m}(-1)^{2R_z/a}\cos\phi_{\mathrm{av}}\cos\left(\frac{2\pi}{a}\,\partial' R_z+\frac{\theta}{2}\right),\end{aligned} \tag{1}$$

where $\phi_{\mathrm{av}}=(\phi_++\phi_-)/2$ is the average phase, and $\theta=\phi_+-\phi_-$ is the phase difference. Here $\alpha_s=-2\hbar V/UN$ is the constant of proportionality for a system with N atoms in volume V, and $\hat{m}$ is the spin polarization direction. Because the average phase ϕ_{av} is arbitrary, the overall SDW amplitude $2\alpha_s g\cos\phi_{\mathrm{av}}$ is not determined by our model.

Associated with the rotational invariance of the free energy about the $\hat{m}$ direction, the transverse spin-wave (SW) modes evolve from the satellites at $\mathbf{Q}'_{\pm}$ with the same temperature-independent mode velocity $c=v_F/\sqrt{3}$ as in the C regime. Despite their itinerant origin, SW's in Cr alloys bear many striking similarities to SW's in local-moment rare-earth antiferromagnets. For example, the dynamical susceptibility associated with SW's in Cr has precisely the same functional form as in a local-moment antiferromagnet with nearest-neighbor coupling. This and other evidence suggests that SW's in Cr correspond to the rigid rotation of the spin at every lattice site.

In the C phase, the only Goldstone modes are the transverse SW's. But in the I phase, longitudinal phason modes are associated with the translational invariance of the ISDW state under changes in the phase difference θ. By contrast, shifting the average phase ϕ_{av} would affect the SDW amplitude $g'\equiv g\cos\phi_{\mathrm{av}}$.

At low frequencies, the phasons evolve linearly from the SDW satellites with mode velocity c_{ph}, which is always less than the SW velocity c. We find that c_{ph} approaches c as T approaches T_N, or as the wave-vector mismatch ∂ increases. Unlike the SW modes, the phasons are damped for any nonzero frequency. As the frequency increases, the half-width of the phasons grows, and the inner phason modes bend towards the H point $\mathbf{G}/2=(2\pi/a)(0,0,1)$ midway between the two satellites. At low frequencies below 10 meV, phasons were observed[5] in the longitudinally polarized ISDW phase below 120 K in pure Cr. At about 60 meV, the inner phasons intersect the H point and their cross section reaches a maximum. This effect was recently observed in neutron-scattering measurements by Fukuda *et al.*[8] Above 60 meV, the inner phasons become overdamped and disappear.

Since the magnetic moments are produced by electron-hole pairs, oscillations of the SDW amplitude $\mathbf{g}'=g'\hat{m}$ are allowed above a pair-breaking energy. We find that degenerate transverse *and* longitudinal amplitude modes lie above each satellite, but at a lower frequency than in the C phase. Unlike oscillations of the CSDW amplitude, oscillations of the ISDW amplitude do not decay with time.

A class of collective excitations called wavons is associated with oscillations of SDW wave vectors $\mathbf{Q}'_{\pm}$ about their equilibrium values. Undamped wavon modes lie near the first and third harmonics of the SDW. Wavons are responsible for the strong peak in the satellite cross sections recently observed by Endoh *et al.*[7] between 15 and 20 meV.

Excitations about each satellite are prohibited inside the wedge of (q,ω) phase space bordered by the SW and amplitude modes. However, since the wedges centered at each satellite do not overlap, every point in (q,ω) space corresponds to a quasiparticle transition about one ISDW or the other. So, unlike the C cross sections, the I cross sections do not vanish for any frequency or wave vector.

This paper is divided into four main sections. Section II applies the formalism developed in the previous paper to the I regime. Section III describes the resulting I dynamics, and Sec. IV contains a discussion and conclusion. The Appen-

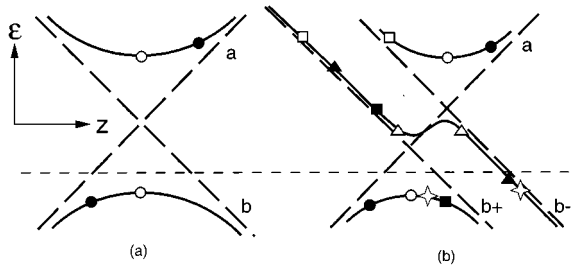

FIG. 1. Paramagnetic (dashed) and hybridized (solid) quasiparticle energies ϵ vs z for the (a) C and (b) I phases. The markers indicate the quasiparticle transitions discussed in the text, and the horizontal dashed line denotes the chemical potential.

dix summarizes our results for the I susceptibilities. Many of the lengthy expressions refered to in the text are contained in paper I.

II. INCOMMENSURATE FORMALISM

Following the method of Young and Sokoloff,[16] we shift the hole energies by the SDW wave vectors: $\epsilon_{b\pm}(\mathbf{k})=\epsilon_b(\mathbf{k}-\mathbf{Q}'_{\mp})$. Above the Néel temperature, the two linearized hole energies plotted by the dashed lines in Fig. 1(b) are separated by the energy $2\kappa\equiv z_0\partial'/\partial$. In the C regime, $\kappa=0$, and the $b\pm$ hole energies plotted in Fig. 1(a) coincide. For simplicity, we assume that the electrons and holes have the same effective mass and the same Fermi velocity v_F. Different effective masses and Fermi velocities would weaken the SDW ordering.

Below the Néel temperature, gaps appear whenever the paramagnetic electron and hole energies cross. In the solid curves of Figs. 1(a) and 1(b), the hybridized electron and hole energies are plotted versus $z=v_F(\mathbf{k}\cdot\hat{n}-k_F)$ near an octahedral face of the electron Fermi surface with normal $\hat{n}$. The chemical potential μ is denoted by a dashed line. We have indexed the hybridized I energies in Fig. 1(b) so that $\epsilon_1\rightarrow\epsilon_a$, $\epsilon_2\rightarrow\epsilon_{b+}$, and $\epsilon_3\rightarrow\epsilon_{b-}$ in the paramagnetic limit $g\rightarrow 0$.

In the C regime, the lower band in Fig. 1(a) is filled with electron-hole pairs. The minimum energy required to break apart an electron-hole pair is the gap energy $2\sqrt{2}g$, which joins the empty circles in Fig. 1(a). In the I regime, two identical gaps appear symmetrically above and below the middle band in Fig. 1(b). For small wave vectors with $|\Delta z|<\kappa$, a minimum energy is still required to traverse each energy gap. But for larger wavevectors with $|\Delta z|\geq\kappa$, quasiparticle transitions are allowed at all frequencies and electron-hole pairs can be broken with no energy cost.

Both the C and I condensates of electron-hole pairs carry zero net momentum with respect to the crystal. Since each C electron-hole pair carries momentum $G/2$, the C condensate must contain an even number of ab pairs. On the other hand, the I condensate must contain the same number of $ab+$ and $ab-$ pairs with total momentum equal to a multiple of $\mathbf{Q}'_+ + \mathbf{Q}'_- = \mathbf{G}$. Correspondingly, the SDW's at $\mathbf{Q}'_+$ and $\mathbf{Q}'_-$ are superposed with equal weight, as assumed in Eq. (1).

As in paper I, we restrict consideration to fluctuations with wavevectors $\mathbf{q}$ parallel to the SDW wave vectors $\mathbf{Q}'_{\pm}=(G/2)(0,0,1\pm\partial')$. So a quasiparticle transition with momentum change $\mathbf{q}=q\hat{z}$ corresponds to a change in z of $\Delta z=v_F\hat{n}\cdot\mathbf{q}=cq\ \mathrm{sgn}(k_z)$, which is the origin of the factor $\sqrt{3}$ in the SW velocity $c=v_F/\sqrt{3}$.

In the absence of a magnetic field, all six I satellites around $\mathbf{G}/2$ or $(0,0,1)$ will be occupied with equal weight. So besides the domain with wave vectors $(0,0,1\pm\partial')$, two other domains will develop with wave vectors $(\pm\partial',0,1)$ and $(0,\pm\partial',1)$. The contribution of these other four satellites to the cross sections along the z axis is difficult to evaluate because it involves fluctuations with wave vectors at all possible angles to the SDW wave vectors. Those contributions are neglected in this paper. So when all three domains are present, our quantitative predictions for the transverse and longitudinal cross sections along the z axis would be inaccurate but the same spectrum of collective modes would appear around all six magnetic satellites. If an I alloy is cooled in a magnetic field parallel to $\hat{z}$, then only the z domain will be occupied and the cross sections evaluated in this paper should be valid.

The transverse and longitudinal susceptibilities contain two sets of contributions centered around each of the two ordering wave vectors $\mathbf{Q}'_{\pm}$:

$$\chi_t(\mathbf{q},\omega)=2[\chi_-(\mathbf{q}-\mathbf{w},\omega)+\chi_-(-\mathbf{q}-\mathbf{w},\omega)], \tag{2}$$

$$\chi_l(\mathbf{q},\omega)=\chi_+(\mathbf{q}-\mathbf{w},\omega)+\chi_+(-\mathbf{q}-\mathbf{w},\omega), \tag{3}$$

$$\chi_\pm(\mathbf{q},\omega)=\chi_1(\mathbf{q},\omega)+\overline{\chi_2}(\mathbf{q},\omega)\pm[\overline{\chi_6}(\mathbf{q},\omega)+\overline{\chi_8}(\mathbf{q},\omega)]. \tag{4}$$

In Eqs. (2) and (3), $\mathbf{q}=q\hat{z}$ is measured from $\mathbf{G}/2$, midway between the two satellites, and $\mathbf{w}=(2\pi/a)(0,0,\partial')$ is the wave vector from $\mathbf{G}/2$ to $\mathbf{Q}'_+$. While the first terms in Eqs. (2) and (3) produce the satellite at $\mathbf{Q}'_+$, the reflected terms with $\mathbf{q}\rightarrow-\mathbf{q}$ produce the satellite at $\mathbf{Q}'_-$. Just as in the C regime, the difference in sign between the transverse and longitudinal susceptibilities arises from the relation $G^{\uparrow\uparrow}_{ab\pm}=-G^{\downarrow\downarrow}_{ab\pm}$ between ''anomalous'' Green's functions.

The notation used in Eq. (4) is a shorthand for the susceptibilities $\chi^{(\sigma_1\sigma_2)}_{ijop}(\mathbf{q},\omega)$ defined by Eqs. (15a)–(15b) of paper I and represented graphically in Fig. 3 of paper I. The barred susceptibilities $\overline{\chi_i}$ are obtained from the unbarred quantities χ_i with the change $b\pm\rightarrow b\mp$. For example, $\chi_1(\mathbf{q},\omega)=\chi^{\uparrow\uparrow}_{aab+b+}(\mathbf{q},\omega)$ and $\overline{\chi_1}(\mathbf{q},\omega)=\chi^{\uparrow\uparrow}_{aab-b-}(\mathbf{q},\omega)$. Because the $b+$ and $b-$ energies are translated by wave vectors $\mathbf{Q}'_-$ and $\mathbf{Q}'_+$, the crystal momentum carried by $\chi_1(\mathbf{q},\omega)=\chi^{\uparrow\uparrow}_{aab+b+}(\mathbf{q},\omega)$ is $\mathbf{p}=\mathbf{q}-\mathbf{Q}'_-$ and the crystal momentum carried by $\overline{\chi_1}(\mathbf{q},\omega)=\chi^{\uparrow\uparrow}_{aab-b-}(\mathbf{q},\omega)$ is $\mathbf{p}=\mathbf{q}-\mathbf{Q}'_+$. The momenta of the susceptibilities in Eqs. (2) and (3) are shifted by $\pm\mathbf{w}$, so that each term transfers the same crystal momentum.

Finally, the transverse and longitudinal cross sections σ_t and σ_l are defined by

$$\sigma_t=U^2N(0)(n+1)\mathrm{Im}\chi_t(\mathbf{q},\omega), \tag{5a}$$

$$\sigma_t=U^2N(0)(n+1)\mathrm{Im}\chi_l(\mathbf{q},\omega), \tag{5b}$$

where $n=1/[\exp(\beta\omega)-1]$ is the Boltzmann function and $N(0)$ is the single-spin density of states of either the electron or hole Fermi surface (assumed identical). Above T_N, the susceptibilities $\chi_6(\mathbf{q},\omega)$ and $\chi_8(\mathbf{q},\omega)$ vanish so that

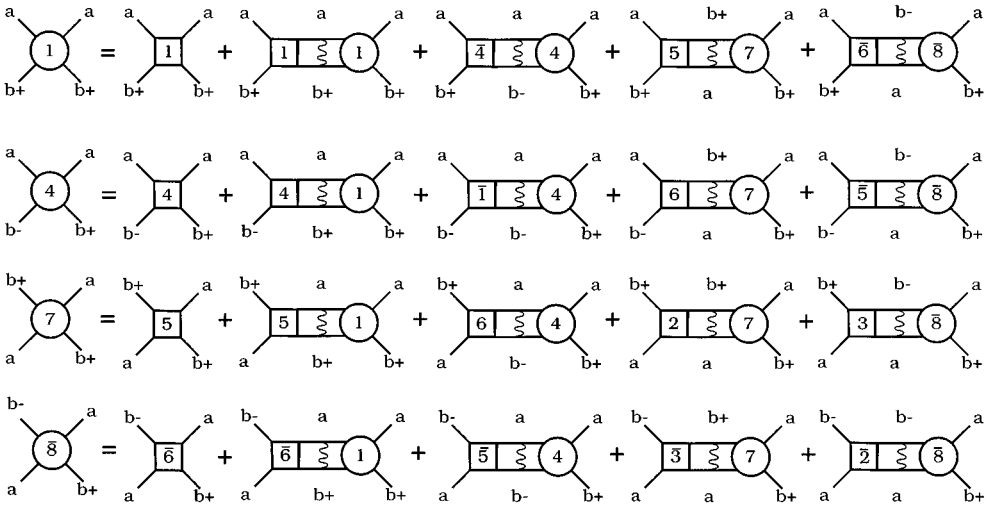

FIG. 2. Graphical representation of the coupled equations for $\chi_1(\mathbf{q},\omega)$, $\chi_4(\mathbf{q},\omega)$, $\chi_7(\mathbf{q},\omega)$, and $\chi_8(\mathbf{q},\omega)$.

$\chi_+(\mathbf{q},\omega)=\chi_-(\mathbf{q},\omega)$. Hence $\chi_t(\mathbf{q},\omega)=2\chi_l(\mathbf{q},\omega)$, $\sigma_t=2\sigma_l$, and the spin fluctuations are isotropic.

Each susceptibility in Eq. (4) can be described by the quasiparticles which enter or leave a vertex. While χ_1 and $\overline{\chi_2}$ correspond to $ab+$ or $ab-$ pairs passing through the vertex, $\overline{\chi_6}$ and $\overline{\chi_8}$ correspond to both $ab+$ and $ab-$ pairs entering the vertex and joining the condensate. Since each $ab\pm$ pair carries momentum $\mathbf{Q}'_{\pm}=\mathbf{G}-\mathbf{Q}'_{\mp}$, these susceptibilities change the momentum of the condensate by a multiple of $\mathbf{G}$. In other words, the momentum entering each of these correlation functions from the right of Fig. 3 in paper I equals the momentum exiting from the left, to within a multiple of $\mathbf{G}$.

Other correlation functions change the momentum of the condensate by a nontrivial amount. For example, the susceptibility $\chi_4(\mathbf{q},\omega)=\chi^{\uparrow\uparrow}_{aab-b+}(\mathbf{q},\omega)$ corresponds to an $ab+$ pair entering the vertex from the right and an $ab-$ pair exiting from the left. So the momentum entering $\chi_4(\mathbf{q},\omega)$ from the the right is $\mathbf{p}=\mathbf{q}-\mathbf{Q}'_-$ while the momentum exiting from the left is $\mathbf{p}=\mathbf{q}-\mathbf{Q}_+$. In the C regime, these momenta are equal and $\chi_4(\mathbf{q},\omega)$ enters the susceptibilities of Eqs. (26) and (27) in paper I. But in the I phase, $\chi_4(\mathbf{q},\omega)$ must gain momentum $\mathbf{Q}'_- - \mathbf{Q}'_+ = -2\mathbf{w}$ from the condensate in order to transform an incoming $ab+$ pair into an outgoing $ab-$ pair. As implied by the definition of the spin-spin correlation function in Eq. (12) of paper I, only terms with the same incoming and outgoing momenta may contribute to the transverse and longitudinal susceptibilities. So correlation functions $\chi_3(\mathbf{q},\omega)$, $\chi_4(\mathbf{q},\omega)$, $\chi_5(\mathbf{q},\omega)$, and $\chi_7(\mathbf{q},\omega)$ must be omitted from Eqs. (2) and (3) for the I susceptibilities.

Consequently, the C dynamics *cannot* be recovered from the $\partial'\to 0$ limit of the I dynamics. In the C phase, any fluctuation which changes the number of electron-hole pairs by an even number is permitted. But in the I phase, spin fluctuations must maintain the same number of $ab+$ and $ab-$ pairs. So a fluctuations which transforms an $ab+$ into an $ab-$ pair through a process like $\chi_4(\mathbf{q},\omega)$ is prohibited.

Nonetheless, the ladder diagrams for $\chi_1(\mathbf{q},\omega)$, $\overline{\chi_2}(\mathbf{q},\omega)$, $\overline{\chi_6}(\mathbf{q},\omega)$, and $\overline{\chi_8}(\mathbf{q},\omega)$ do involve these forbidden susceptibilities. After expanding each susceptibility in a series of ladder diagrams, we find that the two subsets $\{\chi_1, \chi_4, \chi_7, \overline{\chi_8}\}$ and $\{\overline{\chi_2}, \chi_3, \overline{\chi_5}, \overline{\chi_6}\}$ do not couple to each other. The first set of four coupled equations are

$$\chi_1=\chi_1^{(0)}+\chi_1^{(0)}U\chi_1+\overline{\chi_4^{(0)}}U\chi_4+\chi_5^{(0)}U\chi_7+\overline{\chi_6^{(0)}}U\overline{\chi_8}, \tag{6a}$$

$$\chi_4=\chi_4^{(0)}+\chi_4^{(0)}U\chi_1+\overline{\chi_1^{(0)}}U\chi_4+\chi_6^{(0)}U\chi_7+\overline{\chi_5^{(0)}}U\overline{\chi_8}, \tag{6b}$$

$$\chi_7=\chi_5^{(0)}+\chi_5^{(0)}U\chi_1+\chi_6^{(0)}U\chi_4+\chi_2^{(0)}U\chi_7+\chi_3^{(0)}U\overline{\chi_8}, \tag{6c}$$

$$\overline{\chi_8}=\overline{\chi_6^{(0)}}+\overline{\chi_6^{(0)}}U\chi_1+\overline{\chi_5^{(0)}}U\chi_4+\overline{\chi_3^{(0)}}U\chi_7+\overline{\chi_2^{(0)}}U\overline{\chi_8}, \tag{6d}$$

which uses the relations $\chi_8^{(0)}=\chi_6^{(0)}$ and $\chi_7^{(0)}=\chi_5^{(0)}$ between the Hartree-Fock (HF) susceptibilities $\chi_i^{(0)}(\mathbf{q},\omega)$. The second set of coupled equations is obtained with the transformations $1\leftrightarrow 2$, $3\leftrightarrow 4$, $5\leftrightarrow 7$, and $6\leftrightarrow 8$.

The first set of equations is represented graphically in Fig. 2, where the Coulomb interaction $U>0$ is drawn as a wiggly line, the full susceptibilities χ_i as circles, and the HF susceptibilities $\chi_i^{(0)}$ as squares. Although terms like $\chi_4^{(0)}$ and $\chi_5^{(0)}$ enter Eqs. (6a) and (6d) for χ_1 and $\overline{\chi_8}$, contributions such as $\overline{\chi_4^{(0)}}U\chi_4^{(0)}$ and $\overline{\chi_5^{(0)}}U\chi_4^{(0)}$ maintain the same incoming and outgoing momenta and do not change the momentum of the condensate. The solutions for $\chi_t(\mathbf{q},\omega)$ and $\chi_l(\mathbf{q},\omega)$ are summarized in the Appendix. As in the C phase, the imaginary susceptibilities are proportional to the factor $1/U^2N(0)$, which is canceled by the prefactors to the cross sections in Eqs. (5a) and (5b).

The HF susceptibilities $\chi_i^{(0)}(\mathbf{q},\omega)=\phi_1^{(i)}(\mathbf{q},\omega)+i\phi_2^{(i)}(\mathbf{q},\omega)$ were evaluated in Appendixes B and C of paper I. As shown in Appendix C of paper I, the imaginary part $\phi_2^{(i)}(\mathbf{q},\omega)$ sums all quasiparticle transitions between branches j and k, satisfying the momentum-conservation condition

$$\Delta z=z_j(v^*)-z_k(v^*-\omega)=cq. \tag{7}$$

For every allowed quasiparticle transition, each imaginary susceptibility contains an integral of the form

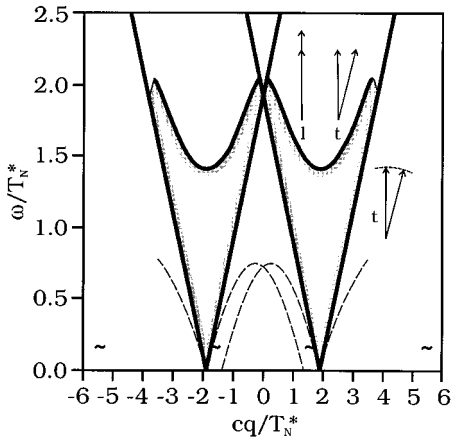

FIG. 3. The collective modes of I Cr with $cw/T_N^\star=\kappa/T_N^\star\approx 1.903$ are plotted in the bold lines with $z_0/T_N^\star=4.7$ and $T/T_N=0.5$. Excitations about each SDW are only allowed outside the hashed region. Damped longitudinal excitations are plotted in the dashed lines. The dynamics of individual spins are pictured for the SW and amplitude modes.

$$\int dv\ F(v)\delta[z_j(v)-z_k(v-\omega)-cq]=\left.\frac{F(v)}{|dg_{jk}/dv|}\right|_{v^*}, \tag{8}$$

where $g_{jk}(v)\equiv z_j(v)-z_k(v-\omega)$. The frequencies v^* and energies z_i satisfying Eq. (7) were solved analytically in Appendix A of paper I.

When quasiparticle transitions join energies with the same slope, $dg_{jk}/dv=0$ and $\phi_2^{(i)}(\mathbf{q},\omega)=\pm\infty$. Such a transition is called *enhanced*. For example, an enhanced transition joins the filled circles of Fig. 1(a). An enhanced quasiparticle transition may be associated with either a zero or a divergence in the full transverse and longitudinal susceptibilities. In many instances, a divergence in one susceptibility is accompanied by a zero in the other. Because nearby transitions also have very small denominators dg_{jk}/dv, the most important enhanced transitions are between quasiparticle energies with zero slope $d\epsilon/dz=0$, such as between the empty circles in Fig. 1(a).

A spin excitation with wave vector $\mathbf{q}$ and frequency ω about the $\mathbf{Q}'_\pm$ SDW corresponds to quasiparticle transitions with wave-vector change $\xi_\pm\equiv c(q\mp w)$ and energy change ω. Incoherent spin excitations about each SDW are only possible outside the wedge of $(\mathbf{q},\omega)$ phase space centered at either $\mathbf{Q}'_+$ or $\mathbf{Q}'_-$, and bordered by the hashed marks in Fig. 3. In this figure, $T_N^\star\approx 80$ meV is the fictitious Néel temperature of a perfectly nested alloy with $\partial=0$. Inside the left or right wedge of Fig. 3, fluctuations about $\mathbf{Q}'_-$ or $\mathbf{Q}'_+$ are prohibited and the imaginary HF susceptibilities $\phi_2^{(i)}(\mathbf{q}\pm\mathbf{w},\omega)$ vanish. For example, a spin excitation with wave vector $\mathbf{q}=\mathbf{w}$ about the $\mathbf{Q}'_+$ SDW corresponds to a vertical quasiparticle transition with $\xi_+=0$. This transition is only possible when ω exceeds the gap energy of $1.41T_N^\star$ in Fig. 3. For sufficiently large $|\xi|/T_N^\star\geq\kappa$ beyond the sides of the wedge, quasiparticle transitions are possible at all frequencies.

For the remainder of this paper, we reserve the notation ξ/c for the momentum $q\pm w$ measured relative to one of the two SDW wave vectors. In the transverse or longitudinal susceptibilities, the wave vector $\mathbf{q}$ is measured from $\mathbf{G}/2$, midway between the two satellites. On the other hand, the crystal momentum $\mathbf{p}$ is given by $\mathbf{q}+\mathbf{G}/2$.

After the two wedges centered at $\mathbf{Q}'_+$ and $\mathbf{Q}'_-$ are superimposed as in Fig. 3, each point in $(\mathbf{q},\omega)$ phase space is associated with an excitation about at least one of the two ordering wave vectors. Points lying outside both wedges are associated with excitations about both ISDW's. So in contrast to the C regime, the neutron-scattering cross sections are nonzero for all frequencies and wave vectors. Above T_N, the wedges collapse and the incoherent spin excitations produce the paramagnetic background predicted theoretically[9,20] and observed experimentally.[21,22]

By adding the contributions from each SDW, Eqs. (2) and (3) allow us to distinguish the collective modes about one SDW from the collective modes about the other. Using the results of the Appendix, the longitudinal $(+)$ or transverse $(-)$ collective modes about $\mathbf{Q}'_+$ are given by the poles of

$$\chi_\pm(\mathbf{q}-\mathbf{w},\omega)=-\frac{2}{U}+\frac{1}{t_{1\pm}(\mathbf{q}-\mathbf{w},\omega)+it_{2\pm}(\mathbf{q}-\mathbf{w},\omega)}, \tag{9}$$

where $t_{1\pm}+it_{2\pm}=U^2D/N_\pm$. Both the denominator D and the numerators $N_\pm=N_\pm^a+N_\pm^b$ are evaluated in the Appendix. The excitations about $\mathbf{Q}'_-$ are given by the same expression as Eq. (9) with $\mathbf{q}\rightarrow-\mathbf{q}$.

Collective modes about either ISDW state are determined by the zeros of the denominator $D(\xi,\omega)$. Unlike the numerators $N_\pm(\xi,\omega)$, $D(\xi,\omega)=D(-\xi,\omega)$ is an even function of the relative wave vector ξ. So if the numerators are nonzero, the collective modes will be symmetric about each SDW wave vector. Since the same denominator appears in both the transverse and longitudinal susceptibilities, the collective modes will also be degenerate unless one set of numerators vanishes.

Because $\chi_{t,l}(\mathbf{q},\omega)$ sums the contributions about each ISDW, the collective modes about $\mathbf{Q}'_+$ are not affected by the quasiparticle transitions about $\mathbf{Q}'_-$. This does not imply, however, that the dynamics of the two SDW's are independent. Within the three-band model, quasiparticle transitions are allowed from one condensate to the other. For example, the $\overline{\chi_4^{(0)}}U\chi_4^{(0)}$ term in χ_1 involves the transfer of a hole from the $ab-$ to the $ab+$ condensates and then back to the $ab-$ condensate with no net change in momentum. In the two-band model, such processes are forbidden, and the dynamical coupling between the two SDW's is lost.

If $t_{2\pm}$ vanishes faster than $t_{1\pm}$, then the transverse or longitudinal collective mode about the SDW at $\mathbf{Q}'_\alpha$ $(\alpha=\pm)$ is associated with a δ function in the imaginary susceptibility $\mathrm{Im}\chi_\pm(\alpha\mathbf{q}-\mathbf{w},\omega)$. As discussed in paper I, the integrated strength s of this collective mode is proportional to $(d\omega/dq)^{-1}$. So the weight of any collective mode diverges when the slope $d\omega/dq$ vanishes. The same conclusion holds for damped excitations with $t_{2\pm}<0$. The half-width of a damped excitation is given by $\Delta q\propto t_{2\pm}/|d\omega/dq|$, which vanishes as $t_{2\pm}\rightarrow 0$ but diverges as $d\omega/dq\rightarrow 0$.

The cross sections σ_t and σ_l defined by Eqs. (5a) and (5b), include both the incoherent background of spin fluctuations and the collective modes. To distinguish those two sets of contributions, we define the incoherent cross sections σ_{it} and σ_{il} by subtracting the δ-function contributions of the

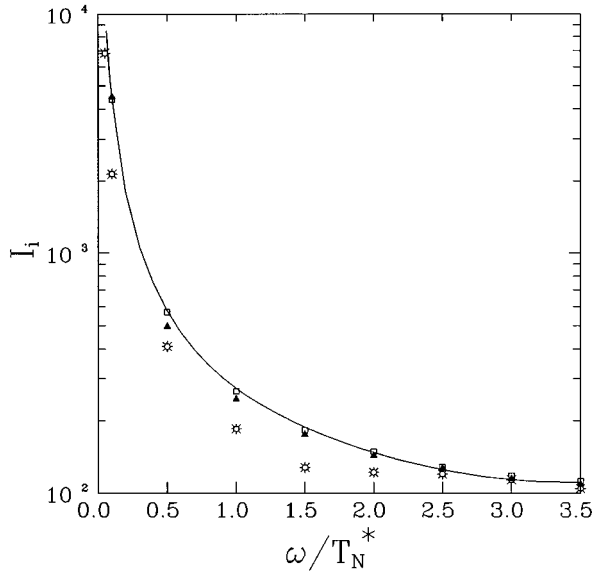

FIG. 4. The incoherent I background $I_i=I_{it}+I_{il}$ vs normalized frequency $\omega/T_N^\star$ for $T=0.5T_N$ (stars), 0.9 (triangles), 0.975 (squares), or 1 (solid line) and $z_0/T_N^\star=4.7$.

collective modes from σ_t and σ_l. For comparison with the C results, we also define the total cross section $\sigma=\sigma_t+\sigma_l$ and the total incoherent cross section $\sigma_i=\sigma_{it}+\sigma_{il}$. Then the total and incoherent backgrounds I and I_i are obtained by integrating the total or incoherent cross sections σ or σ_i over wave vector cq.

III. INCOMMENSURATE DYNAMICS

Because the summation over the I quasiparticle transitions cannot be performed exactly, the imaginary susceptibilities $\phi_i^{(2)}(\mathbf{q},\omega)$ are more complicated than their C counterparts. Evaluating the real susceptibility $\phi_i^{(1)}(\mathbf{q},\omega)$ using the Kramers-Kronig relation requires a numerical integration over the imaginary susceptibility, with some attached numerical uncertainty. So the I cross sections are more difficult to evaluate, and contain greater numerical errors than the C cross sections evaluated in paper I.

In Fig. 4, we plot the total incoherent background I_i, versus frequency for four different temperatures. Like the C background plotted in Figs. 8 and 10 of paper I, the I background also grows as T approaches T_N and diverges as ω approaches 0. But unlike the C background, which increases with frequency above the energy gap, the I background decreases monotonically. The limiting paramagnetic background with $T=T_N$ is plotted in the solid curve.

As revealed by Fig. 4, the integrated background diverges more strongly than the thermal factor $n+1\rightarrow T/\omega$ as $\omega\rightarrow 0$. In paper I, we were able to show analytically that the C background I_i, diverges like $(n+1)/\omega\propto T/\omega^2$ as $\omega\rightarrow 0$. Although such an analytic result has not been verified, we believe that the I background also behaves in this fashion.

The complex quasiparticle energies of the I phase produce a rich spectrum of collective excitations. Since Fig. 1(b) contains five segments of quasiparticle energies, there are 25 types of I transitions, far greater than the four types of transitions in the C phase. As discussed in Sec. I, the collective modes may be associated with fluctuations of the SDW polarization direction $\hat{m}$, amplitude g', phase difference θ, and wave vectors $\mathbf{Q}'_{\pm}$. While the SW and amplitude modes were also present in the C phase, the phason and wavon modes have no analog in the C dynamics.

A. Spin-wave modes

The invariance of the free energy under rotations of the spin-polarization direction $\hat{m}$ is associated with transverse Goldstone modes evolving from each satellite. These SW modes have a linear dispersion $\omega=cq$ with the same temperature-independent mode velocity $c=v_F/\sqrt{3}$ as in the C phase. Each SW mode borders the side of a wedge inside of which quasiparticle transitions about that satellite are forbidden. Along the side of the wedge, each imaginary HF susceptibility $\phi_2^{(i)}(\xi,\omega)$ vanishes at the frequency $\omega=|\xi|$. Inside the quasiparticle continuum above the top of the wedge, the individual imaginary HF susceptibilities become nonzero, but $\mathrm{Im}(\chi_1+\overline{\chi_2}-\overline{\chi_6}-\overline{\chi_8})$ still vanishes at $\omega=|\xi|$, so the SW mode remains undamped.

These results disagree sharply with previous authors,[9,10] who neglected the coupling between the two condensates of electron-hole pairs. Using a two-band model, Sato and Maki[9] found that the SW velocity vanishes at the Néel temperature and at the triple point. Starting with a one-dimensional array of local moments with long-range exchange interactions, Wolfram and Elliatioglu[10] obtained a spectrum of multiple branches and energy gaps with modes originating from $q=0$ as well as from the SDW ordering wave vectors.

Unfortunately, experimental fits to the twin ''chimneys'' evolving from the I satellites are even more difficult than fits to the single ''chimney'' of the C phase. Measurements by Mikke and Jankowska[2] on a CrRe alloy indicated a SW velocity of 500 meV Å, about half of the C value[23,24] and one third of the theoretical value $c\approx 1500$ meV Å. We shall return to this discrepancy in Sec. IV.

As discussed in paper I, the strength $s_t=32\pi g^2(n+1)/\omega$ of each SW in the C phase has precisely the same form as for a Heisenberg antiferromagnet.[25] Motivated by this relation, we have searched for a similar result in I alloys. While an analytic expression has eluded us, the ISW strength is given numerically by

$$s_t=(n+1)\,\frac{A_t g^2}{\omega}, \tag{10}$$

where $A_t\approx 16\pi/3$ is independent of frequency, temperature, and mismatch energy z_0. This remarkable relation again underscores the similarity between SW's in itinerant and local-moment antiferromagnets. As expected, the SW strength vanishes as $T\rightarrow T_N$ or as $\omega\rightarrow\infty$.

Comparing C and I expressions, we find that the combined weight of the four ISW's evolving from the satellites at $(0,0,1\pm\partial')$ is approximately three times smaller than the weight of the two CSW's evolving from (0,0,1). However, the intensity of the SW's evolving from each magnetic satellite along the z axis may have a different angular dependence on $\mathbf{q}\cdot\hat{z}$ than the intensity of the SW's in the C phase. In the C limit $\partial'\rightarrow 0$, the total integrated intensity of the ISW's evolving from $\mathbf{Q}'_{\pm}$ must smoothly approach the integrated intensity of the CSW's evolving from $\mathbf{G}/2$. So most of

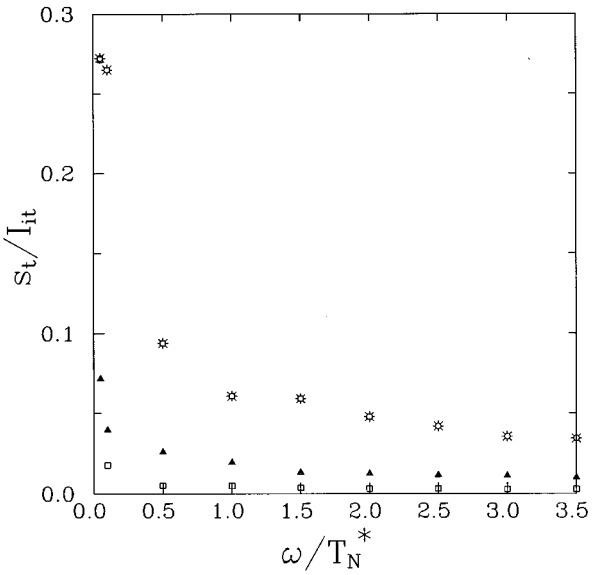

FIG. 5. The relative SW strength $s_t/I_{\rm it}$ vs $\omega/T_N^\star$ for the same parameters as in Fig. 4.

the ISW intensity must develop in the q_x and q_y directions, perpendicular to the ordering wave vectors. Of course, a complete description of the SW ''cones'' evolving from each satellite must include fluctuations with wave vector $\mathbf{q}$ nonparallel to $\mathbf{Q}'_\pm$. We shall attempt such a general description in future work.

In paper I, we argued that SW's in a C alloy involve the rigid rotation of each spin about its equilibrium value. Now in the I regime, the two SW's with frequency ω and crystal momentum $p=\pm Q'_\alpha+\omega/c$ $(\alpha=\pm)$ have an identical strength s_t. This suggests that the spin deviation at site $\mathbf{R}$ should be written

$$\delta S(\mathbf{R},t)\propto S_{0\alpha}(\mathbf{R})\exp\{i(\mathbf{p}\mp\mathbf{Q}'_\alpha)\cdot\mathbf{R}-i\omega t\}, \qquad (11)$$

which also yields the rigid rotation of each spin.

Figure 5 compares the SW strength with the weight of the transverse, incoherent background $I_{\rm it}$. As in the C phase, the relative SW strength decreases with increasing temperature and vanishes at T_N. Comparing Fig. 5 with Fig. 11 of paper I reveals that the relative weights of the SW modes are an order of magnitude smaller than in the C regime. So the I background contains a much larger fraction of the spin fluctuations than does the C background. If the incoherent background diverges like $(n+1)/\omega$ as $\omega\rightarrow 0$, then $s_t/I_{\rm it}$ should approach a constant in this limit.

In recent work, Lorenzo *et al.*[6] used the form of Eq. (10) to fit the low-temperature $(T/T_N\leqslant 0.3)$ and low-frequency $(\omega/T_N^*\leqslant 0.15)$ transverse susceptibility of pure Cr. At such low frequencies and temperatures, Fig. 5 indicates that the combined weight of the four SW's is somewhat larger than the incoherent transverse background. Hence the observed constancy of $\omega I_t/(n+1)\approx 4A_t g^2$ below 100 K reflects the weak temperature dependence of the order parameter below about $0.7T_N$. Since the incoherent background falls off more weakly with increasing frequency than does the SW strength $s_t\sim 1/\omega$, the incoherent background $I_{\rm it}$ will eventually dominate the SW's, and this simple parametrization of the transverse susceptibility will break down.

B. Amplitude modes

Due to their high frequency and small weight, amplitude modes have never been observed in an itinerant antiferromagnet, to our knowledge. Nonetheless, they are of great theoretical interest due to their absence in local-moment antiferromagnets. Amplitude modes about an ISDW state were first predicted within a two-band model by Sokoloff.[26] Later, Lee, Rice, and Anderson[27] and Psaltakis[12] confirmed the existence of amplitude modes for one-dimensional systems.

Within the three-band model for itinerant antiferrogmagnets, degenerate transverse and longitudinal modes lie symmetrically on either side of each SDW wave vector and just below the top of each wedge. Near $\mathbf{G}/2$, the amplitude modes smoothly join one of the SW modes from the far satellite. On the other side of $\mathbf{Q}'_\pm$, the amplitude modes tangentially enter the quasiparticle continuum. In the C limit $\partial'\rightarrow 0$, the SW cones centered at $\mathbf{Q}'_+$ and $\mathbf{Q}'_-$ merge into $\mathbf{G}/2$, and the I amplitude modes are squeezed into a vanishing portion of phase space. The C amplitude mode with frequency $2\sqrt{2}g$ at $q=0$ first appears as a large longitudinal absorption peak between the two I satellites (see Sec. II G below). So the I amplitude modes do *not* evolve into the C amplitude mode discussed in paper I.

Unlike the C amplitude mode, the I amplitude modes are slightly displaced below the quasiparticle continuum. For the parameters of Fig. 3, the I amplitude modes lie at a frequency of about $1.4\times 10^{-4}T_N^*$ below the top of each wedge. Consequently, the I amplitude modes are associated with δ functions in the transverse and longitudinal susceptibilities. So, unlike oscillations of the CSDW amplitude, oscillations of the ISDW amplitude do not decay with time.

The weight of each amplitude mode is about ten times smaller than the weight of a SW mode with the same frequency. Unlike the strengths of the SW modes, the strengths of the transverse and longitudinal amplitude modes are different on either side of each satellite. Directly above each satellite, the transverse weight is twice the longitudinal weight. Close to $\mathbf{G}/2$, the transverse mode dominates; near the outside of each SW cone, the longitudinal and transverse weights are roughly equal.

In an itinerant antiferromagnet, deformations of the SDW amplitude $\mathbf{g}'=\hat{m}g\cos\phi_{\rm av}$ can be produced by either transverse or longitudinal fluctuations. Exactly at the satellite wave vectors $\mathbf{Q}'_+$ or $\mathbf{Q}'_-$, the degeneracy of the amplitude modes can be explained with a simple picture. Longitudinal fluctuations of magnitude $\gamma S_{0\pm}(\mathbf{R})\exp(i\omega t)$ cost condensation energy $\Delta F\propto\langle\mathbf{S}\cdot\mathbf{S}^*\rangle-\mathbf{S}_{0\pm}\cdot\mathbf{S}^*_{0\pm}=(\gamma|S_{0\pm}|)^2$. On the other hand, a purely transverse excitation with crystal momentum $\mathbf{p}=\mathbf{Q}'_+$ or $\mathbf{Q}'_-$ and magnitude $\gamma S_{0\pm}(\mathbf{R})\exp(i\omega t)$ will rock all the spins back and forth with the same time-dependent angle. Due to the absence of any bending energies, transverse fluctuations at $\mathbf{R}$ will also cost condensation energy $(\gamma|S_{0\pm}|)^2$. Hence the longitudinal and transverse amplitude modes are degenerate. At $\mathbf{Q}'_+$ or $\mathbf{Q}'_-$, both collective excitations are standing-wave modulations of the ISDW amplitude which do not affect the nodes of the SDW.

Away from the SDW ordering wave vectors, the transverse amplitude modes must gain a longitudinal component (just as the transverse SW modes have a longitudinal component) so that the combined bending and condensation energies of the transverse mode equals the energy of the purely longitudinal one. As a result, the standing-wave patterns will be disrupted and the nodes of the static SDW will be disturbed.

C. Phason modes

Whereas SW's are associated with the rotational invariance of the free energy, phasons are associated with its translational invariance under a shift in the phase difference θ. Phason modes of a CDW were first predicted by Overhauser.[28] While studied primarily in one-dimensional organic conductors,[29] phasons have also been predicted[5,12] in *I* Cr alloys. For the CSDW state discussed in paper I, fluctuations of the phase difference θ generate fluctuations of the SDW amplitude. So the CSDW state does not support phason modes.

In an *I* alloy, phason modes are produced by the dynamics of the phase difference $\theta(\mathbf{R},t)$ in Eq. (1). Supposing θ_0 to be the equilibrium phase difference and setting $\delta\theta(\mathbf{R},t) = \theta(\mathbf{R},t) - \theta_0$, the change in spin is given by

$$\delta\mathbf{S}(\mathbf{R},t) = -\alpha_s g \hat{m}(-1)^{2R_z/a}\cos\phi_{\rm av}\,{\rm Im}\,\delta\theta(\mathbf{R},t) \times \exp\left\{ i\left(\frac{2\pi}{a}\,\partial' R_z + \frac{\theta_0}{2}\right)\right\}, \tag{12}$$

parallel to $\hat{m}$. Consequently, the phasons are longitudinal excitations which evolve from the SDW wave vectors at $\mathbf{Q}'_{\pm}$.

Like amplitude modes, phasons are also associated with the longitudinal oscillation of the spin $\mathbf{S}(\mathbf{R},t)$ about its equilibrium value. While electron-hole pairs are broken on some lattice sites, they reform on others. So a phason mode transfers electron-hole pairs from one atom to another down the length of the SDW. By contrast, amplitude modes transfer electron-hole pairs into and out of the condensate.

At zero frequency, the poles in the longitudinal susceptibility $\chi_l(\mathbf{q},0)$ at $\mathbf{q}=\pm\mathbf{w}$ are undamped with $t_{1+}(0,0) = t_{2+}(0,0) = 0$. But at any nonzero frequency, the phason modes are damped with $t_{2+}(\xi,\omega)<0$. Below about $0.4T_N^\star$, the phason modes evolve linearly and symmetrically on either side of the satellites at $\mathbf{Q}'_+$ and $\mathbf{Q}'_-$. For all values of temperature and mismatch z_0, the phason mode velocity $c_{\rm ph}$ at zero frequency is smaller than the SW mode velocity $c = v_F/\sqrt{3}$. As shown in Fig. 6, $c_{\rm ph}$ only approaches the SW velocity at the Néel temperature. Also notice that the phason velocity increases with the mismatch energy z_0 or, equivalently, with the V concentration in CrV alloys.

By contrast, Psaltakis[12] used a linear-response formalism in one dimension to conclude that $c_{\rm ph}=c$ ($c=v_F$ in one dimension) at zero temperature. Psaltakis also found that the electron-electron and hole-hole Coulomb repulsion enhances the phason mode velocity. As discussed below, the nesting and ordering wave vectors coincide in the one-dimensional, single-band model used by Psaltakis. So the result $c_{\rm ph}=c$ is recovered in the $z_0\to\infty$ or $Q'_\pm\to Q_\pm$ limit of our model.

At nonzero frequencies, the inner phasons curve outward towards $\mathbf{G}/2$. At a frequency of about $0.75T_N^\star \approx 60$ meV and at a wave vector close to $\mathbf{G}/2$, the slopes $d\omega/dq$ of the inner phasons vanish. As shown in Fig. 3, the inner phason modes then smoothly join the damped longitudinal excitations discussed in Sec. III D. Above $0.75T_N^\star$, the overdamped phason modes disappear. With V doping, the inner phasons will survive to larger energies. For example, when $z_0/T_N^\star = 10$, the inner phasons become overdamped at a much higher energy of $2.65T_N^\star \approx 212$ meV. Psaltakis[12] did not evaluate the dispersion of the phason modes at nonzero frequencies.

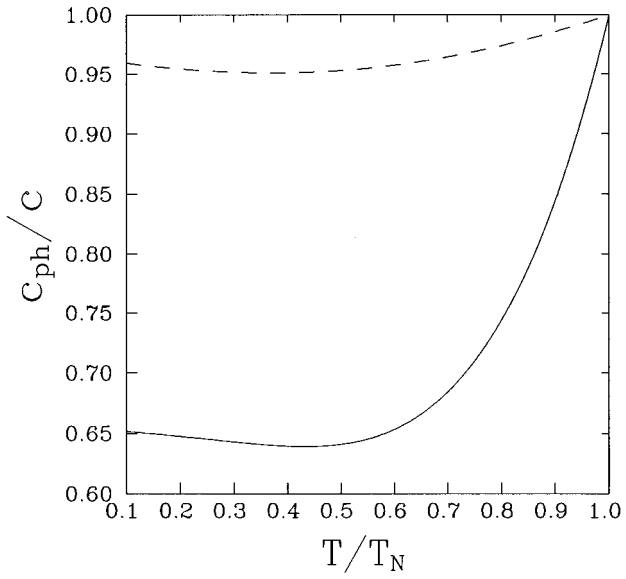

FIG. 6. The phason mode velocity $c_{\rm ph}$ normalized by the SW velocity vs T/T_N for $z_0 T_N^\star = 4.7$ (solid) or 7.0 (dashed).

Fitting the strength of each phason mode to the form of Eq. (10), we find that

$$s_{l\pm} = (n+1)\,\frac{A_{l\pm}(\omega) g^2}{\omega}, \tag{13}$$

where $\pm$ refers to the inner $(-)$ or outer $(+)$ branch. The coefficients $A_{l\pm}$ are now functions of frequency, temperature, and mismatch. In Fig. 7, we plot the ratios $s_{l\pm}/s_t = A_{l\pm}/A_t \approx 3A_{l\pm}/16\pi$ versus frequency for $z_0/T_N^\star = 4.7$ and two different temperatures. For each temperature, the upper set of points corresponds to the inner coefficient $A_{l-}(\omega)$. At zero frequency, $A_{l+}(0) \approx A_{l-}(0)$ depends mainly on the energy mismatch z_0 and only weakly on temperature. For the parameters of Fig. 7, $A_{l\pm}(0) \approx 12.8$, so that the strength of each longitudinal phason mode is only about 0.75 times smaller than the strength of each transverse SW mode with its two possible polarizations. As the mismatch z_0 increases, $A_{l\pm}(0)$ decreases, so the phasons become weaker compared to the SW's. While $A_{l-}(\omega)$ monotonically increases with frequency, $A_{l+}(\omega)$ initially decreases with frequency.

The $(n+1)/\omega \approx T/\omega^2$ divergence of $s_{l\pm}(\omega)$ as $\omega\to 0$ characterizes the Goldstone modes of a SDW. Other damped longitudinal excitations discussed below also evolve from zero-frequency poles in the imaginary susceptibility. However, the strengths of those excitations diverge like the Boltzmann factor $n+1 \approx T/\omega$. So the SW and phason modes dominate the low-frequency response of Cr alloys.

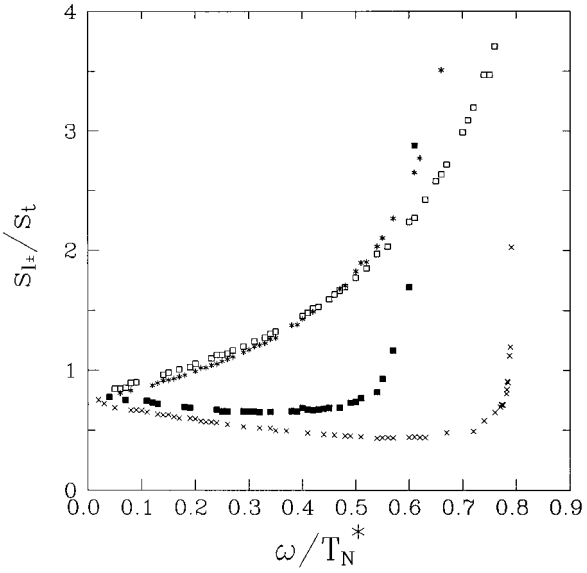

FIG. 7. The phason mode strengths $s_{l\pm}$ normalized by the SW strength s_t vs $\omega/T_N^\star$ for $T/T_N=0.5$ (stars and x's) or 0.8 (squares) and $z_0/T_N^\star=4.7$. The inner phason $(-)$ corresponds to the upper set of points; the outer phason $(+)$ to the lower set.

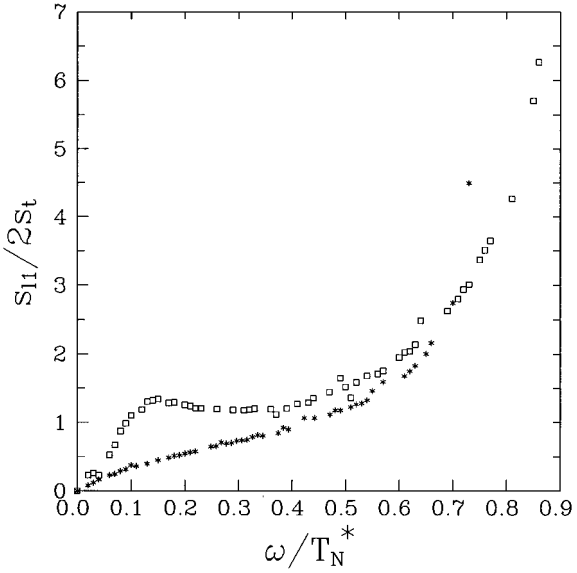

FIG. 8. The strength of the longitudinal damped excitation s_{l1} near the first harmonics $Q'_\pm$ relative to the strength $2s_t$ of the two nearby SW's for the same parameters as Fig. 7.

As discussed at the end of Sec. II, the strength of any damped excitations is inversely proportional to its slope $d\omega/dq$. So the coefficient A_{l-} of the inner phason diverges when it meets the damped longitudinal excitation pictured in Fig. 3. Likewise, the coefficient A_{l+} of the outer phason also diverges, although more weakly, as its slope vanishes.

Unlike the SW modes, the phasons are not associated with δ functions of the susceptibility, and form a part of the incoherent background. Hence the phason mode strength of Eq. (13) is already counted as part of the longitudinal background. At frequencies less than about $0.1T_N^\star$ and temperatures below about $0.5T_N$, the phason modes dominate the rest of the incoherent longitudinal background. Since the longitudinal amplitude modes lie at a much higher frequency, the low-frequency longitudinal intensity may be approximated by $I_l \approx I_{il} \approx 2(s_{l+}+s_{l-})$.

Because they evolve from satellite wave vectors and have velocities close to c, phason modes have been mistaken for SW's. For example, the low-frequency, longitudinal excitations observed by Burke *et al.*[5] were actually phason modes rather than SW's. Recently, Lorenzo *et al.*[6] used the form of Eq. (13) with a single coefficient $A_l=(A_{l+}+A_{l-})/2$ to fit the low-temperature longitudinal susceptibility of pure Cr. For the low frequencies and temperatures studied by Lorenzo *et al.*,[6] the phason modes dominate the rest of the longitudinal background. So, as expected, the scaled longitudinal intensity

$$\frac{\omega}{n+1}\, I_l \approx \frac{2\omega}{n+1}\,(s_{l+}+s_{l-}) = 4A_l(\omega)g^2 \qquad (14)$$

is almost independent of temperature. According to Fig. 7, the sum $A_{l+}(\omega)+A_{l-}(\omega)$ is a weakly *increasing* function of ω below about $0.25T_N^\star \approx 20$ meV. By contrast, Lorenzo *et al.* observe a dramatic falloff of $\omega I_l/(n+1)$ with frequency below about 10 meV. As discussed later, our model is not sophisticated enough to describe this low-frequency behavior.

D. Damped excitations near the first harmonic

As shown in Fig. 3, the damped longitudinal excitations which extend beyond the phasons reach zero frequency close to the first harmonics of the SDW. The zero-frequency pole in the imaginary longitudinal susceptibility at these wave vectors corresponds to the $\xi=\xi_0$ quasiparticle transition between the empty triangles in Fig. 1(b). Translating ξ_0 by $\pm cw$, the longitudinal poles lie at wave vectors $cq=cw\pm\xi_0$ and $-cw\pm\xi_0$, where $cw=\kappa$ and $\xi_0<2\kappa$. As $T\to T_N$, $\xi_0\to 2\kappa$, and the poles merge with the first $\pm cw=\pm\kappa$ and third $\pm 3cw=\pm 3\kappa$ harmonics of the SDW. To distinguish these longitudinal excitations from the phason modes, we label them as excitations $l1$ and $l3$.

Unlike the Goldstone modes, the strengths of excitations $l1$ and $l3$ diverge like $n+1\approx T/\omega$ as $\omega\to 0$. Compared to the phasons, their relative weights $s_{l1}/s_{l\pm}$ and $s_{l3}/s_{l\pm}$ vanish like ω as $\omega\to 0$. So these longitudinal excitations become unobservable at low frequencies.

As ω increases, the wave vector of excitation $l1$ bends towards $G/2$ and approaches the inner phason mode. The longitudinal excitations $l1$ and the inner phasons meet with zero slope $d\omega/dq=0$. So the weights of both excitations diverge at precisely the same frequency. Just below this frequency, the strengths s_{l1} and s_{l-} are nearly equal.

At very low frequencies, s_{l1} is much smaller than the combined weight $2s_t$ of the two nearby SW's. But as shown in Fig. 8, $s_{l1}/2s_t$ rapidly increases with frequency and eventually diverges as the slope $d\omega/dq$ vanishes. Using the parameters in Fig. 3, $s_{l1}/2s_t=1$ when $\omega/T_N^\star \approx 0.4$ and $s_{1l}/2s_t\to\infty$ as $\omega/T_N^\star\to 0.75$. Consequently, the SW cones emanating from each satellite will tilt inward towards $\mathbf{G}/2$, as first observed by Fincher and co-workers.[4] At a frequency of

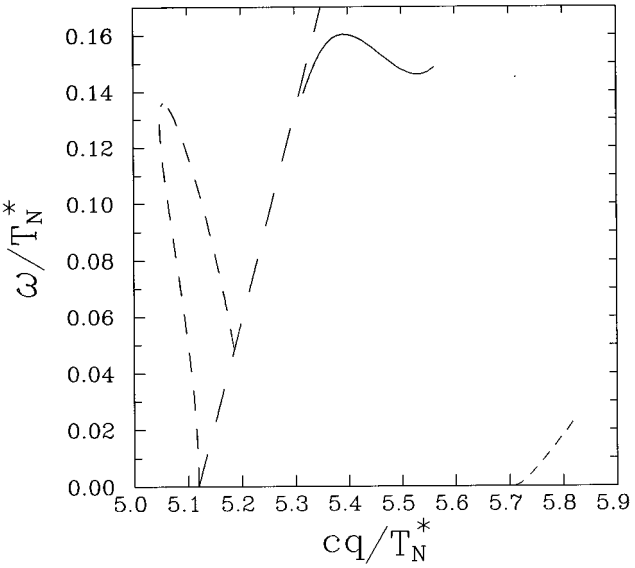

FIG. 9. The wavon mode (solid) and damped longitudinal excitations (medium and short dash) for $z_0=4.7T_N^\star$ and $T/T_N=0.5$. The long dashed line corresponds to the quasiparticle transitions between the filled triangles in Fig. 1(b).

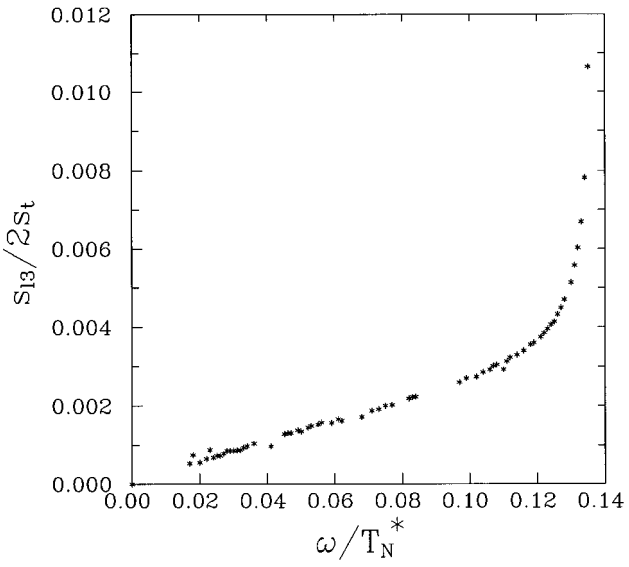

FIG. 10. The strength of the longitudinal damped excitation (medium dashed line with the smaller wavevector in Fig. 9) s_{l3} relative to the SW strength $2s_t$ vs $\omega/T_N^\star$ for the same parameters as Fig. 9.

30 meV, Fincher and co-workers observed that the axis of the SW cones were 30% closer to $G/2$ than at zero frequency. Since the tilting angle will increase with frequency, their result is in good agreement with our estimate for $0.75T_N^\star \approx 60$ meV. As discussed below, the divergence of s_{l1} and s_{l-} near $G/2$ has been recently observed by Fukuda *et al.*[8]

E. Damped excitations near the third harmonic

The zero-frequency quasiparticle transition between the empty triangles in Fig. 1(b) also produces the damped longitudinal excitation $l3$ close to the observed third-harmonics[18] of the SDW at $cq=\pm 3\kappa$. Its frequency is plotted versus wave vector in the medium-dashed lines of Fig. 9, where the long-dashed line corresponds to the enhanced quasiparticle transitions between the filled triangles of Fig. 1(b). So excitation $l3$ begins and terminates at an enhanced quasiparticle transition. For frequencies between $0.045T_N^\star$ and $0.135T_N^\star$, the real denominator has two zeros near $cq=\pm 3\kappa$, so $l3$ has two branches.

A static third harmonic of the SDW was not included in the ''canonical'' inverse Green's function of Eq. (9) of paper I. So, not unexpectedly, the normalized weight $s_{l3}/2s_t$ vanishes as $\omega\rightarrow 0$. Hence, like excitation $l1$, excitation $l3$ is not a Goldstone mode, and disappears at low frequencies. But as shown in Fig. 10 for the $l3$ branch with the smaller wave vector, the relative weight $s_{l3}/2s_t$ diverges at a frequency of about $0.135T_N^\star$, where its slope $d\omega/dq$ vanishes. Above $0.135T_N^\star$, excitation $l3$ is overdamped and disappears.

Another set of poles in the longitudinal susceptibility is induced by the $\omega=0$ quasiparticle transition between the empty squares in Fig. 1(b). For large energies, the wave vector ξ of this transition approaches 2κ. Translating by the satellite wave vectors $\pm cw$, these poles coincide with the first and third harmonics of the SDW. But unlike the SW and phason poles, these poles are not associated with Goldstone modes: their weights diverge like $1/\omega$ rather than $1/\omega^2$ as $\omega\rightarrow 0$. At nonzero frequencies, these longitudinal excitations are damped.

Since it lies very close to the phason pole, the damped excitation evolving from the first harmonic is probably impossible to observe. The damped excitation evolving from the third harmonic survives only at very low frequencies and is much weaker than the $l3$ excitation discussed above. Its dispersion is given by the short-dashed line of Fig. 9. As $T\rightarrow T_N$, $\xi_0\rightarrow 2\kappa$ and the two zero-frequency poles near the third harmonic merge into one.

So even in the absence of a static third harmonic, I alloys remain susceptible to the formation of a dynamically driven third harmonic. But unlike the Goldstone modes, this excitation disappears at low frequencies. Of course, a rigorous theory for the excitations evolving from $cq=\pm 3\kappa$ must incorporate the static third harmonics of the SDW. Only then would the excitations evolving from $\pm 3\kappa$ be true Goldstone modes of the alloy.

F. Wavon modes

In addition to the three classes of collective modes (SW's, amplitude modes, and phasons) discussed above, another class of collective modes is associated with oscillations of the SDW wave vectors $\mathbf{Q}'_\pm$. Unlike the ordering wave vector $Q=2k_F$ of a one-dimensional organic conductor,[29] the SDW wave vectors $\mathbf{Q}'_\pm$ of Cr are not fixed by a nesting condition. Instead, $\mathbf{Q}'_\pm$ are chosen to minimize the free energy, which involves a compromise between the nesting on both sides of the Fermi surfaces. The wavon modes are then produced by oscillations of the ordering wavevectors within this potential well.

For the ISDW state of Eq. (1), the wavon modes correspond to oscillations in the wave-vector parameter ∂' about

its equilibrium value. A small change in ∂' either stretches or contracts the SDW along the z direction. As the change in ∂' vanishes, the original SDW is smoothly restored. By contrast, even a small change in the wave vector of a CSDW state will dramatically change the spin configuration. Whereas the equilibrium CSDW contains spins with values $S_0(\mathbf{R})=\pm\alpha_s g'$ on different sublattices, the nonequilibrium CSDW would contain spins with all possible values between $\alpha_s g'$ and $-\alpha_s g'$. Hence even a vanishingly small change in the CSDW wave vector produces a very large change in free energy. For this reason, wavon modes were not present in the C dynamics discussed in paper I.

As shown in Fig. 3 for $\omega/T_N^\star\approx 0.15$, the inner wavons (each both longitudinal and transverse) join the inner SW's, while the outer wavons (purely longitudinal) lie close to the third harmonics. Although within the quasiparticle continuum, the wavons are undamped. The wavon modes are produced by zeros of the susceptibility denominator $D(\xi,\omega)$ with $\xi\approx\pm 2\kappa$. Because the longitudinal numerator $N_+(\xi,\omega)$ is nonzero at these wave vectors and frequencies, the longitudinal wavons lie symmetrically on either side of the SDW satellites. But near the third harmonic, the zeros in $D(\xi,\omega)$ are canceled by zeros in the transverse numerator $N_-(\xi,\omega)$, so the outer wavons are purely longitudinal. Since the same pole is responsible for both, the transverse and longitudinal wavons near the first harmonic are degenerate.

While the longitudinal wavons are easy to understand, the transverse wavons near the first harmonic involve the coherent oscillation of both the wave-vector parameter ∂' and the polarization direction $\hat{m}$. If the change in ∂' is $\delta\partial'(\mathbf{R},t)$ and the change in polarization direction is $\delta\mathbf{m}(\mathbf{R},t)$ perpendicular to $\hat{m}$, then the transverse fluctuation of the spin on site $\mathbf{R}$ can be written

$$\delta\mathbf{S}(\mathbf{R},t)=2\alpha_s g(-1)^{2R_z/a}\cos\phi_{\rm av}\mathrm{Re}\,\delta\mathbf{m}(\mathbf{R},t)\times\exp\left\{i\left(\frac{2\pi}{a}[\partial'+\delta\partial'(\mathbf{R},t)]R_z+\frac{\theta}{2}\right)\right\}. \tag{15}$$

This combination of infinitesimals is possible because $\delta\mathbf{S}(\mathbf{R},t)$ cannot be linearized in $\delta\partial'$. As $\delta\partial'/\delta m\to 0$, this excitation becomes a SW mode. Correspondingly, the inner wavons terminate at a SW branch.

The transverse and longitudinal wavon modes near the first harmonic are plotted versus wave vector for several temperatures in Fig. 11. Using the symmetry of $D(\xi,\omega)$ about $\xi=0$, the longitudinal wavons near the third harmonic are obtained from Fig. 11 with the operation $cq\to -cq+2\kappa$. Since the inner wavons terminate on a SW branch, the outer wavons terminate at the point $cq=3\kappa-\omega$. Figure 12 plots the termination frequency of the inner wavons versus temperature. This termination point coincides with the onset of quasiparticle transitions between branches 2 and 3, such as between the open stars in Fig. 1(b).

With increasing temperature, the range of frequencies and wave vectors of the wavons collapses. In the limit $T\to T_N$, the wavon frequency vanishes and the modes disappear. As the temperature decreases, the wavon frequency increases and the undamped wavons are again confined to a shrinking window of wavevectors. Below about $0.2T_N$, the undamped

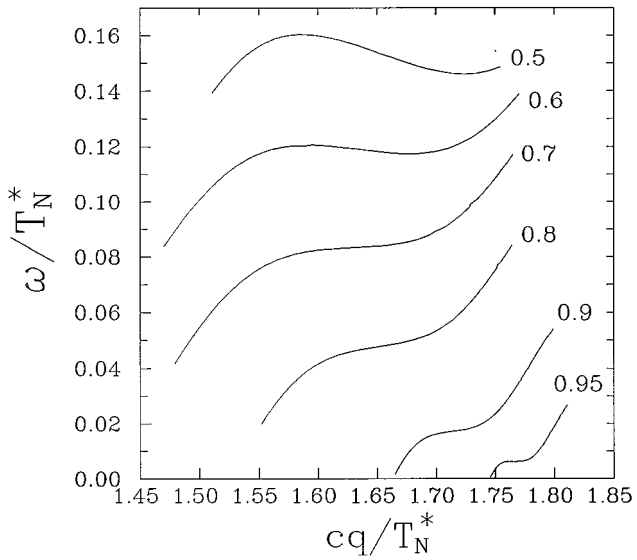

FIG. 11. The transverse and longitudinal wavons near the first harmonic for $z_0=4.7T_N^\star$ and the various temperatures T/T_N given. The dispersion of the longitudinal wavon near the third harmonic is obtained with the operation $cq\to -cq+2\kappa$.

wavons are replaced by a set of damped excitations. Excitations to the left of the circles in Fig. 12 are damped.

For any energy mismatch z_0, the range of wave vectors of the wavon modes is always less than the difference $\Delta Q=Q_+-Q'_+=2\pi(\partial-\partial')/a$ between the nesting and SDW wave vectors. As $z_0\to\infty$, $\partial'\to\partial$ and the range of wave vectors of the wavon modes vanishes. As shown in Fig. 12, the wavon mode frequency also vanishes as $z_0\to\infty$. In the C limit, $\partial'\to 0$, the wavons are again restricted to a vanishing window in wave-vector space. As remarked above, the CSDW state does not support wavons.

The longitudinal wavon near the third harmonic is plotted

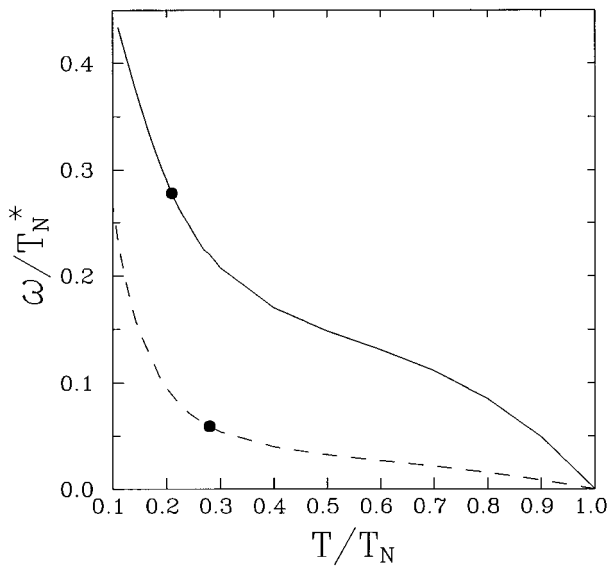

FIG. 12. The intersection frequency of the wavons with the inner SW branch vs temperature T/T_N for $z_0/T_N^\star=4.7$ (solid) or 7 (dashed). The wavons are damped to the left of the circles.

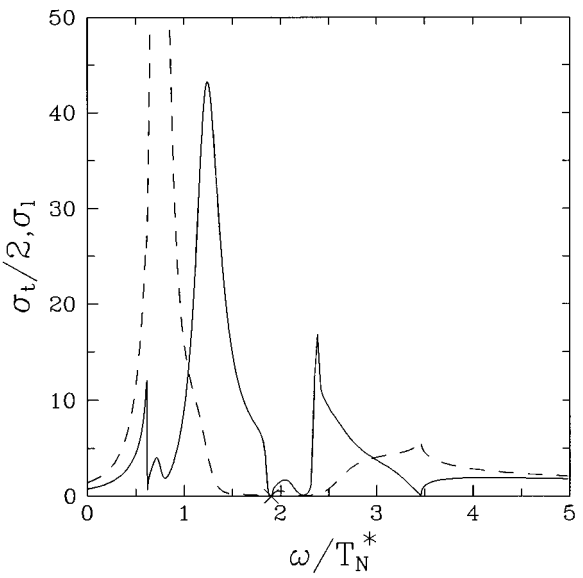

FIG. 13. The transverse (solid) and longitudinal (dash) I cross sections vs $\omega/T_N^\star$ for $q=0$. $z_0/T_N^\star=4.7$, and $T=0.5T_N$. The SW δ functions are denoted by an X.

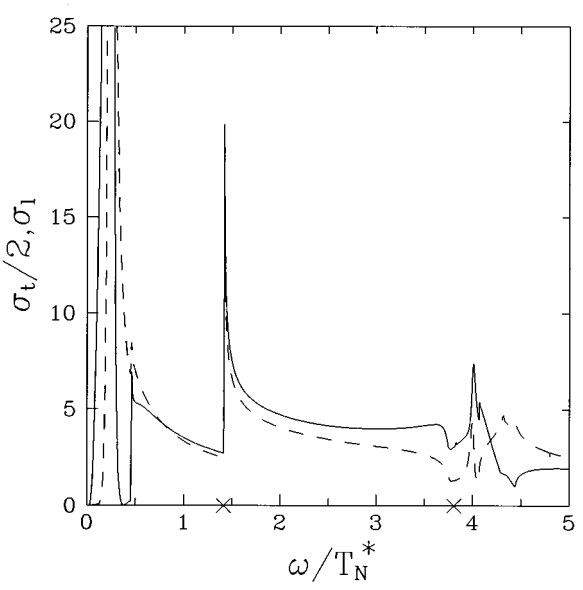

FIG. 14. Same as Fig. 13, but with $q=\pm w$. The SW and amplitude modes are denoted by X's.

in the solid curve of Fig. 9 for $T/T_N=0.5$ and $z_0/T_N^\star=4.7$. As shown, the wavon evolves tangentially from the dashed line of enhanced quasiparticle transitions, such as between the filled triangles in Fig. 1(b).

Remarkably, the inner wavons were recently observed by Endoh *et al.*[7] as a peak in the satellite intensity between 15 and 20 meV at 54 K. For $T/T_N=0.2$ and $z_0/T_N^\star=4.7$, Fig. 12 indicates that the satellite intensity should be strongly peaked at about $0.28T_N^\star\approx 23$ meV. However, electron-phonon scattering may lower this frequency by suppressing the SDW order parameter g. As shown in Fig. 12, our model predicts that the peak frequency will decrease rapidly with increasing temperature and with V doping. Thus future measurements may be able to confirm the existence of this interesting class of collective excitations. Because the strength of the longitudinal wavons is much smaller than that of the transverse wavons, it is unlikely that the outer wavons can be detected.

G. Cross sections

Fixing $\mathbf{q}=0$ or $\mathbf{p}=(G/2)(0,0,1)$, we plot the transverse and longitudinal cross sections versus frequency in Fig. 13. Fluctuations about each SDW contribute equally to the excitations at $q=0$. Since quasiparticle transitions with relative wave vectors $\xi_\mp=c(q\pm w)=\pm\kappa$ are allowed at all frequencies, the cross sections remain nonzero even at $\omega=0$. The strong longitudinal peak at $\omega/T_N^*\approx 0.75$ is produced by the phason and $l1$ excitations discussed in Secs. III C and III D. Intraband transitions across the chemical potential are responsible for the large transverse peak at $\omega/T_N^*\approx 1.3$. Two SW modes cross at $\omega/T_N^*=\kappa/T_N^*\approx 1.903$, which is denoted by an X. Because their widths are infinitesimally small, the SW and amplitude-mode δ functions do not appear in the plots of the transverse and longitudinal cross sections. The peak in the transverse cross section at $\omega/T_N^*=2.39$ is produced by the enhanced transition across the energy gap between the filled squares in Fig. 1(b).

At higher energies still, the longitudinal peak near $3.46T_N^*$ is driven by the enhanced transition between the filled circles on the top and bottom bands in Fig. 1(b). In the C limit, this peak evolves into the C amplitude mode, which is associated with the transition between the filled circles in Fig. 1(a). Above $3.46T_N^*$, no additional enhanced transitions arise, and the cross sections are smooth functions of frequency. In the limit $\omega/T_N^*\to\infty$, the fluctuations become isotropic, and the transverse cross section is exactly twice the longitudinal cross section.

In Fig. 14, $\mathbf{q}=\mathbf{w}$ is fixed at the right-hand satellite with crystal momentum $\mathbf{p}=(G/2)(0,0,1+\partial')$. While quasiparticle transitions about $\mathbf{Q}'_+$ have a relative wave vector $\xi_+=c(q-w)=0$, transitions about $\mathbf{Q}'_-$ have a relative wave vector $\xi_-=c(q+w)=2\kappa$. Because $\xi=0$ transitions are forbidden below the top of the wedge, excitations below the energy gap of $1.41T_N^*$ are associated with fluctuations about the far satellite at $\mathbf{Q}'_-$. Since $q=w$ is an ordering wave vector, the SW and phason δ functions lie at $\omega=0$.

At very low frequencies, quasiparticle transitions with $\xi=2\kappa$ lie far from the chemical potential, and the background cross sections are small. The low-frequency peaks in the satellite cross sections at $\omega=0.24T_N^*\approx 19$ meV are produced by damped excitations which evolve from the wavons between the two SW's. Because these damped excitations increase in frequency as they cut across the satellite wave vector, the peak frequency of $0.24T_N^*$ is larger than the wavon frequency of $0.15T_N^*$ obtained from Fig. 12 for $T/T_N=0.5$.

Just below the energy gap, the amplitude-mode δ function is marked by an X. Whereas only longitudinal fluctuations diverge above the C energy gap in Fig. 12 of paper I, both transverse and longitudinal fluctuations diverge above the I gap in Fig. 14. The SW δ function at $\omega/T_N^*=2\kappa/T_N^*=3.806$ is also denoted by an X. As expected, the fluctuations become isotropic at high frequencies with $\sigma_t=2\sigma_l$.

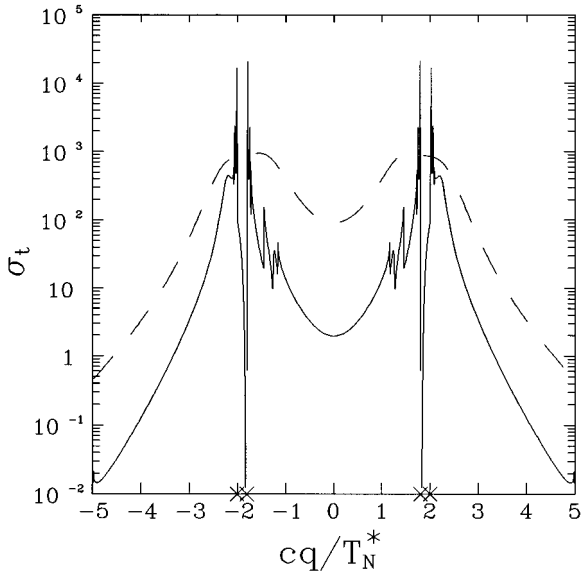

FIG. 15. The transverse cross section vs $cq/T_N^\star$ for $\omega/T_N^\star=0.1$, $z_0/T_N^\star=4.7$, and $T/T_N=0.5$ (solid) or 1 (dashed). Each SW δ function is denoted by an X.

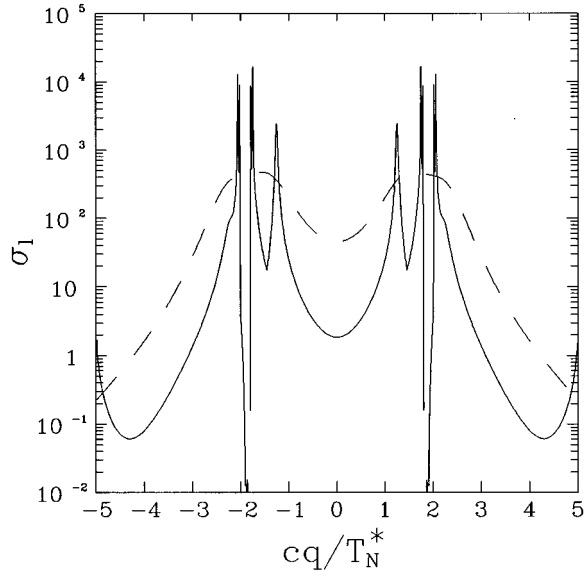

FIG. 16. The longitudinal cross section vs $cq/T_N^\star$ for the same parameters as Fig. 15.

While each feature in Figs. 13 and 14 can be associated with the onset of quasiparticle transitions, the dynamical susceptibility will be dominated by the three largest peaks. At $q=0$, the other features in Fig. 13 are dwarfed by the large longitudinal peak at $0.75T_N^*\approx 60$ meV and by the smaller transverse peak at $1.3T_N^*\approx 104$ meV. As discussed in Sec. IV, the larger peak at 60 meV was recently observed by Fukuda *et al.*[8] The dominant peak in the satellite cross section at $0.24T_N^*\approx 19$ meV is associated with the wavon modes, which were recently observed by Endoh *et al.*[7] Unfortunately, the smaller features in Figs. 13 and 14, such as the onset of amplitude fluctuations at $1.41T_N^*$ in Fig. 13, may be unobservable.

When $\omega=0$, the SW and phason poles at $cq=\pm cw$ carry infinite weight. So the elastic cross sections are dominated by the satellite peaks. The transverse and longitudinal cross sections for $\omega=0.1T_N^*\approx 8$ meV are plotted in Figs. 15–17. In all three figures, the cross sections with $T/T_N=0.5$ are plotted on the solid curve, and the paramagnetic cross sections with $T=T_N$ are plotted on the long-dashed line. If each of the three magnetic domains is occupied, then Figs. 15 and 16 will underestimate the cross sections near $q=0$ or $\mathbf{p}=\mathbf{G}/2$, close to all six satellites. In contrast to the rather simple paramagnetic cross sections first obtained by Sato and Maki,[9] the magnetic cross sections are spectroscopic fingerprints of the allowed quasiparticle transitions. Notice that the magnetic cross sections fall off more rapidly with wave vector than does the paramagnetic cross section.

In Fig. 15, the SW poles at $cq/T_N^*=1.903\pm 0.1$ and -1.903 ± 0.1 are denoted by X's. As indicated by Fig. 5, the weight of each SW pole is only about 25% the integrated weight of the incoherent background. Both the transverse and longitudinal cross sections are very small in the wedge of (q,ω) phase space between the SW modes, where only spin fluctuations about the far satellite are permitted. The transverse cross section contains additional peaks associated with the SW modes just outside each wedge. Each phason mode is associated with three zeros of $t_{1+}(\xi,\omega)$, and appears as two distinct peaks in the longitudinal cross section of Fig. 16. The largest and outermost peak was used to assign the phason mode velocity and strength in Sec. III C. The $l1$ excitation discussed in Sec. III D contributes strong peaks at the wave vectors $cq/T_N^*\approx\pm 1.24$ in Fig. 16.

Longitudinal excitations near the third harmonic are plotted in Fig. 17, which includes an additional curve for $T/T_N=0.9$. At low temperatures, the two damped excitations appear as distinct peaks separated by a region with a much smaller cross section. Excitation $l3$ discussed in Sec. III E lies to the left of the weaker dynamically driven third har-

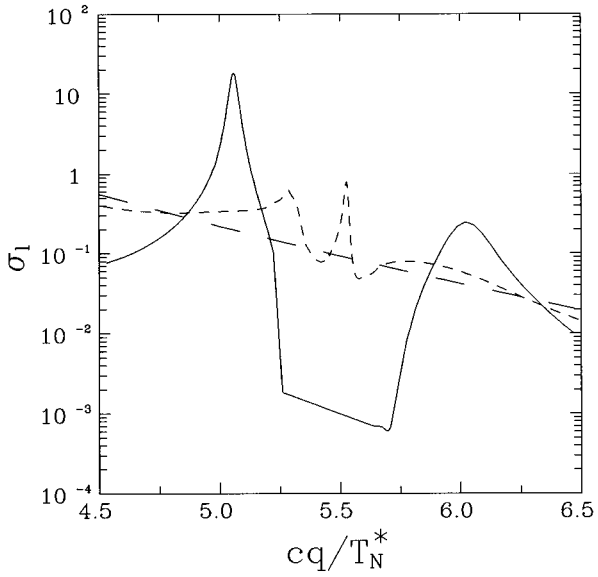

FIG. 17. The longitudinal cross section vs $cq/T_N^\star$ for $T/T_N=0.5$ (solid), 0.9 (short dash), or 1 (long dash). Other parameters as in Fig. 15.

monic. As the temperature increases, $\xi_0 \to 2\kappa$ and the peaks move closer together. The peak heights decrease with increasing temperature and disappear in the paramagnetic limit.

As the frequency increases, the cross sections become more complex due to the larger number of possible quasiparticle transitions. For a fixed frequency, each peak or valley in the cross sections can be associated with one of the 25 possible types of quasiparticle transitions. Of course, most features will be smoothed by quasiparticle damping. At very high frequencies exceeding the gap energy between the lower and upper bands, the satellite peaks in the I cross sections disappear. In this limit, the cross sections also become independent of the energy mismatch z_0 and wavevector parameter κ.

IV. DISCUSSION AND SUMMARY

In this paper, we have examined the excitations about the two ISDW states of pure Cr and CrV alloys. Spin excitations with frequency ω and wave vector $p = q + G/2$ about the ISDW with wave vector $Q'_{\pm} = \pm w + G/2$ are associated with quasiparticle transitions with energy change ω and wavevector change $q \mp w$. While the relatively simple quasiparticle energies of the C phase produced a simple spectrum of collective modes which could be solved analytically, the more complex quasiparticle energies of the I phase produce a richer spectrum of collective excitations which must be solved numerically.

Our basic model for the spin dynamics consists of an electron-hole condensate generated by the Coulomb attraction U. In the I phase, a three-band model couples the $ab+$ and $ab-$ condensates. Although the RPA is the simplest formalism to produce SW modes in a conventional antiferromagnet, applying the RPA to the ''canonical'' model of an itinerant antiferromagnet has been a challenging task. In the I phase, quasiparticle transitions between the three bands of energies produce a wealth of excitations about the two satellites $\mathbf{Q}'_{\pm} = (G/2)(0,0,1 \pm \partial')$.

Surprisingly, the imaginary susceptibilities contain several poles at zero frequency. But only the SW and phason poles at the first harmonics are associated with instabilities of the alloy. While the strengths of the Goldstone modes diverge like $1/\omega^2$, the strengths of the other excitations diverge more weakly like $1/\omega$. Hence the low-frequency dynamics is dominated by the SW and phason excitations. Only at frequencies above about $0.15T_N^* \approx 12$ meV does the rest of the incoherent background become important.

The most disturbing discrepancy between theory and experiment lies in the smaller observed value of the SW velocity. In the I phase, the phason modes will broaden the SW cones, and lower the effective mode velocity in measurements of the total cross section.

A second possibility could also explain the discrepancy in the C phase: the SW mode velocity may depend on the direction of the wavevector $\mathbf{q}$. Fluctuations along the $\hat{z}$ direction are probably stiffer than fluctuations which shear two of the octahedral faces against each other. So the SW velocity with $\mathbf{q}$ parallel to $\mathbf{Q}'_{\pm}$, which was evaluated in this and previous papers, may be larger than for $\mathbf{q}$ parallel to an octahedral face of the Fermi surface. Since the resolution ellipsoid[6] of the neutron-scattering cross section is extended in $(\mathbf{q},\omega)$ space, the measured SW velocity would be lower than $c = v_F/\sqrt{3}$.

It is instructive to compare the spin dynamics of a transition-metal antiferromagnet with the spin dynamics of a one-dimensional organic conductor.[29] For the latter system, the ISDW wave vector $Q = 2k_F$ is fixed by the nesting across the Fermi surface. As mentioned previously. Psaltakis' result[12] for the phason velocity of a one-dimensional ISDW can be recovered in the $z_0 \to \infty$ or $Q'_{\pm} \to Q_{\pm}$ limit of our model. Since the nesting and ordering wave vectors coincide, wavon modes are not present in a one-dimensional organic conductor.

Several workers[30–32] have studied the spin dynamics about an ISDW by starting with a phenomenological expansion of the free energy near T_N in powers of the spin operators $\mathbf{S}(\mathbf{R})$, which are assumed to obey the canonical commutation relations for Heisenberg spins. Due to this assumption, the SW mode velocity is found to scale like the SDW order parameter g and vanish as $T \to T_N$. The amplitude, phason, and wavon excitations all involve the transfer of electron-hole pairs from one atomic site to another or into and out of the condensate. Such processes are forbidden by the assumption that the spin $\mathbf{S}(\mathbf{R})$ obeys canonical commutations rules and is fixed in magnitude. Hence, phenomenological approaches to the I spin dynamics are severely handicapped.

Despite the complexity of the excitation spectrum described in this paper, many important effects are missing, and the resulting spin dynamics is oversimplified. As previously remarked, the ''canonical'' model ignores the higher harmonics of the SDW. Both a CDW with wave vectors $2Q'_{\pm}$ and a third harmonic of the SDW with wave vectors $3Q'_{\pm}$ will generate their own unique dynamics. At $\omega = 0$, the translational invariance of the ICDW produces the observed peaks[17] at the satellite wave vectors $2\mathbf{Q}'_{\pm} = G(0,0,1 \pm \partial')$, on either side of the reciprocal-lattice vector $\mathbf{G}$. The rotational and translational invariance of the third harmonic produces peaks[18] at $3\mathbf{Q}'_{\pm} = (G/2)(0,0,1 \pm 3\partial') + \mathbf{G}$. While transverse SW modes may be associated with the third harmonic, longitudinal phason modes may be associated with the translational invariance of both higher harmonics. By changing the quasiparticle spectrum, both the second and third harmonics will also affect the excitations about the first harmonic of the SDW.

As first realized by Shibatani, Motizoki, and Nagamiya,[33] the ''canonical'' model of Cr alloys assumes that the chemical potential $\mu = -z_0/4$ is unaffected by the formation of a SDW. Since the SDW depletes the electrons from the nested Fermi surfaces, the ''canonical'' model implicitly assumes that an infinite electron reservoir replenishes the electrons transfered to the condensate. If the reservoir is finite, then the chemical potential $\overline{\mu}(T)$ will decrease and the effective mismatch $\overline{z_0}(T) = -4\overline{\mu}(T)$ will increase as the SDW grows. In practice, the electron reservoir contains all bands which do not contribute to the nested electron and hole Fermi surfaces. The reservoir power ρ is defined as the ratio of the reservoir density of states to the electron-hole density of states $\rho_{\mathrm{eh}} = 4N(0)$ for both spins and both Fermi surfaces.

Many authors[34] have studied the effects of a finite reservoir on the phase diagram of Cr alloys. Most recently,[34] we examined the effects of a finite reservoir within the three-

band model of the I phase. Surprisingly, order parameters $\{g_s,\partial_s'\}$ which are saddle points of the ''canonical'' free energy with $\rho=\infty$ may become minima of the free energy when $\rho<\infty$.

Since all fluctuations are infinitesimal, the spin dynamics places no additional demands on the electron reservoir. Hence the excitation spectrum is not directly affected by the size of the electron reservoir, and depends only on the order parameters $\{g,\partial'\}$, the temperature T, and the mismatch energy z_0. But if the reservoir is finite, then the mismatch z_0 must be replaced by the effective mismatch $\overline{z_0}(T)$. So the temperature dependences of the incoherent background, SW strength, and phason velocity will be affected by the temperature dependence of the effective mismatch energy $\overline{z_0}(T)$.

For some values of the reservoir power ρ and mismatch energy $\overline{z_0}(T)$, it may be necessary to use the saddle-point solutions $\{g_s,\partial_s'\}$ rather than the order parameters which minimize the ''canonical'' free energy. With I saddle-point solutions, the peaks in the central band of quasiparticles in Fig. 1(b) disappear. Consequently, the damped longitudinal excitations $l1$ and $l3$ produced by the $\omega=0$ quasiparticle transition across the central band are lost. If 2κ is the smallest energy for a vertical quasiparticle transition, the amplitude mode becomes absorbed into the quasiparticle continuum. Otherwise, two amplitude modes appear. However, the spectrum of Goldstone modes evolving from each satellite remains fundamentally unchanged. In particular, the SW velocity is still given by $c=v_F/\sqrt{3}$, and the phason velocity remains smaller than c. We will examine this case in more detail at a future date.

Because spin-orbit coupling has been neglected, our results do not depend on the angle between the spin-polarization direction $\hat{m}$ and the nesting wave vectors $\mathbf{Q}_\pm=Q_\pm\hat{z}$. However, the spin-orbit energy in pure Cr produces two different I regimes:[1] one transversely (T) polarized above 120 K and the other longitudinally (L) polarized below 120 K. Because the neutron-scattering cross sections only measure spin fluctuations perpendicular to the wave vector $\mathbf{q}$, experimentalists can distinguish longitudinal from transverse spin fluctuations in the I phase (but not in the C phase). In the LSDW phase below 120 K, the cross section across the $\mathbf{p}=(G/2)(0,0,1\pm\partial')$ satellites equals σ_t while the cross section across the $\mathbf{p}=(G/2)(1,0,\pm\partial')$ satellites equals $\sigma_l+\sigma_t/2$.

Below about 4 meV, experiments by Burke *et al.*[5] and Lorenzo *et al.*[6] in the LSDW state indicate that $\sigma_l\gg\sigma_t$. So the low-frequency excitations evolving from the satellite wave vectors at $\mathbf{p}=(G/2)(1,0,\pm\partial')$ must be phasons. In the TSDW state at very low frequencies, Burke *et al.* find that the spin fluctuations are predominantly perpendicular to the ordering wave vectors.[5] Hence the spin-orbit energy constrains the spin fluctuations to lie along the possible polarization directions: parallel to $\mathbf{Q}_\pm'$ and to the magnetic moments in the LSDW state, and transverse to $\mathbf{Q}_\pm'$ in the TSDW state. In future work, we will study this behavior by adding the spin-orbit coupling to our basic model.

The ''commensurate diffuse'' scattering first observed by Fincher, Shirane, and Werner[4] is a broad hump centered at $G/2$ in the TSDW state at a frequency of about 4 meV. But as shown in Fig. 13, the $q=0$ or $\mathbf{p}=(G/2)(0,0,1)$ cross sections remain very small until frequencies of order $0.7T_N^*\approx55$ meV. So the ''commensurate diffuse'' scattering cannot be explained within our basic model. Later work by Burke *et al.*[5] indicated that the ''commensurate diffuse'' peak might be produced by very low-velocity excitations evolving from each satellite. Within our model, the scale for all mode velocities is set by the Fermi velocity $v_F\approx2600$ meV Å. However, the Fincher-Burke excitations have a velocity of approximately 43 meV Å, roughly 60 times smaller than the Fermi velocity and very close to the velocity of a longitudinal acoustic phonon[5] in Cr. Clearly, the Fincher-Burke excitations involve a much smaller velocity scale than contained in our model. It is possible, however, that the Fincher-Burke excitations are produced by the coupling between the ISDW and the acoustic phonons mediated by a CDW. This will also be investigated in future work.

Measurements by Burke *et al.*[5] and Lorenzo *et al.*[6] indicate that the transverse and longitudinal spin fluctuations are averaged above 10 meV. Experimental cross sections above 10 meV should then be compared with the average cross section $\sigma_{\rm av}=(\sigma_t/2+\sigma_l)/2$. Two mechanisms may be responsible for this averaging. At frequencies above 10 meV, the resolution ellipsoid[6] of the experimental measurements may be large enough to average the transverse and longitudinal fluctuations effectively. Alternatively, fluctuations of the electron spins above 10 meV may average the susceptibilities $\chi_{ijop}^{\uparrow\uparrow}(\mathbf{q},\omega)$ and $\chi_{ijop}^{\uparrow\downarrow}(\mathbf{q},\omega)$. Since $\underline{\chi}_\pm$ of Eq. (4) differ only in the spin-dependent terms $\pm(\underline{\chi_6}+\underline{\chi_8})$, the averaged transverse or longitudinal susceptibility are both equal to $(\chi_t/2+\chi_l)/2$. Notice that three times this average cross section $3\sigma_{\rm av}$ differs from the total cross section $\sigma=\sigma_t+\sigma_l$ expected if the spin fluctuations are isotropic. Only at very high frequencies above $3.5T_N^\star$ does $3\sigma_{\rm av}\to\sigma$.

Our results for the average cross section agree well with the recent high-frequency measurements of Endoh *et al.*[7] The observed peak in the satellite intensities between 15 and 20 meV is slightly lower than our estimate for the wavon frequency of $0.28T_N^\star\approx23$ meV. As the temperature increases, we predict that the wavon frequency should decrease and vanish as $T\to T_N$.

Very recently, Fukuda *et al.*[8] observed that the $q=0$ intensity reaches a broad maximum centered at about 60 meV. This observation agrees with the predicted longitudinal peak in Fig. 13 at $0.74T_N^\star\approx59$ meV, where the damped $l1$ excitations intersect $q=0$. Although this peak will broaden with increasing temperature, the peak frequency should change very little in the range $0<T/T_N<0.7$, where the phason mode velocity is relatively constant. At higher temperatures, $c_{\rm ph}$ increases, and the phason peak moves to higher frequencies, as suggested by Figs. 7 and 8. But as the peak width continues to grow, the phason eventually disappears from the averaged cross section. It may also be possible to observe the secondary transverse peak at $1.3T_N^\star\approx104$ meV.

With V doping, the phason velocity $c_{\rm ph}$ of CrV alloys increases, and the $l1$ excitations intersect $q=0$ at a higher energy. So at low temperatures, the 60-meV peak in the $G/2$ cross section should move to higher energies. As indicated by Fig. 12, the wavon peak in the satellite cross section of pure Cr should move downward with V doping.

Other predictions of our model may also be borne out by experiments. Above 10 meV but below $0.75T_N^\star\approx60$ meV, it may be possible to distinguish the SW modes from the

nearby $l1$ excitation. The separation between these excitations should increase with frequency. However, as indicated by Figs. 5 and 8, the strength of the $l1$ excitation may be large enough to observe only very close to $q=0$. The $l3$ excitation may be sufficiently separated from the third harmonic to be observable at low frequencies. As the temperature increases, this excitation should move towards higher wave vectors and eventually merge with the third harmonic. Low-frequency measurements in the LSDW phase may be able to observe the predicted variation of the phason mode velocity with temperature and doping. Unlike the SW modes, the damping energy of the phasons should increase with frequency.

Even the most basic theory for the spin dynamics of Cr alloys produces a rich spectrum of collective modes and excitations. Previous experimental work on the dynamics of Cr alloys was undertaken with very little theoretical guidance. Hopefully, our work will help in the design of future experiments and the development of more refined models.

ACKNOWLEDGMENTS

One of us (R.F.) would like acknowledge support from the U.S. Department of Energy under Contract No. DE-FG06-94ER45519. This work was also sponsored by the U.S. Department of Energy under Contract No. DE-ACO5-96OR22464 with Lockheed Martin Energy Research Corporation. S.L. would like to thank Professor L. Sham and Professor R. Dynes for their hospitality at UCSD. Useful conversations with Dr. Y. Endoh, Dr. E. Fawcett, Dr. B. Sternlieb, Dr. V. S. Viswanath, and Dr. S. Werner are also gratefully acknowledged.

APPENDIX

Our results for the I susceptibilities are summarized in this appendix. Solving the set of four coupled equations in Eqs. (6a)–(6d), we find

$$\chi_1 = -\frac{1}{U} - \frac{1}{U^2}\frac{C\overline{A}-B^2}{A\overline{A}-B^2}. \tag{A1}$$

$$\overline{\chi_8} = -\frac{A(-\chi_2^{(0)\prime}\overline{\chi_6^{(0)}}+\chi_3^{(0)}\chi_5^{(0)})+B(-\chi_2^{(0)\prime}\overline{\chi_5^{(0)}}+\chi_3^{(0)}\chi_6^{(0)})}{A\overline{A}-B^2}, \tag{A2}$$

where we define the convergent susceptibilities

$$\chi_1^{(0)\prime}(\mathbf{q},\omega) = \chi_1^{(0)}(\mathbf{q},\omega) - \frac{1}{U}, \tag{A3a}$$

$$\chi_2^{(0)\prime}(\mathbf{q},\omega) = \chi_2^{(0)}(\mathbf{q},\omega) - \frac{1}{U}, \tag{A3b}$$

and the factors

$$A = \chi_1^{(0)\prime}C + U^2\{-\chi_2^{(0)\prime}\overline{\chi_6^{(0)2}} - \overline{\chi_2^{(0)\prime}}\chi_5^{(0)2} + 2\chi_3^{(0)}\chi_5^{(0)}\overline{\chi_6^{(0)}}\}, \tag{A4a}$$

$$B = -\chi_4^{(0)}C - U^2\{-\chi_2^{(0)\prime}\overline{\chi_5^{(0)}\chi_6^{(0)}} - \overline{\chi_2^{(0)\prime}}\chi_5^{(0)}\chi_6^{(0)} + \chi_3^{(0)}(\chi_5^{(0)}\overline{\chi_5^{(0)}} + \chi_6^{(0)}\overline{\chi_6^{(0)}}), \tag{A4b}$$

$$C = -U^2(\chi_2^{(0)\prime}\overline{\chi_2^{(0)\prime}} + \chi_3^{(0)2}). \tag{A4c}$$

Notice that $\overline{B}=B$ and $\overline{C}=C$ but $\overline{A}\neq A$. The relationships for $\overline{\chi_2}$ and $\overline{\chi_6}$ are obtained with the map $1\leftrightarrow 2$, $3\leftrightarrow 4$, $5\leftrightarrow 7$, and $6\leftrightarrow 8$. As discussed in paper I, $\chi_7^{(0)}(\mathbf{q},\omega)=\chi_5^{(0)}(\mathbf{q},\omega)$ and $\chi_8^{(0)}(\mathbf{q},\omega)=\chi_6^{(0)}(\mathbf{q},\omega)$. Also recall that $\overline{\chi_i^{(0)}}=\chi_i^{(0)}(-\mathbf{q},\omega)$.

So finally putting it all together, we find

$$\chi_\pm \equiv \chi_1 + \overline{\chi_2} \pm (\overline{\chi_6} + \overline{\chi_8}), \tag{A5}$$

$$\chi_1 \pm \overline{\chi_6} = -\frac{1}{U} + \frac{1}{U^2}\frac{N_\pm^a}{D}, \tag{A6a}$$

$$\overline{\chi_2} \pm \overline{\chi_8} = -\frac{1}{U} + \frac{1}{U^2}\frac{N_\pm^b}{D}, \tag{A6b}$$

where

$$\begin{aligned} D = {} & (\chi_2^{(0)\prime}\overline{\chi_2^{(0)\prime}} + \chi_3^{(0)2})(\chi_1^{(0)\prime}\overline{\chi_1^{(0)\prime}} + \chi_4^{(0)2}) - \chi_1^{(0)\prime}\overline{\chi_2^{(0)\prime}}\chi_6^{(0)2} \\ & - \overline{\chi_1^{(0)\prime}}\chi_2^{(0)\prime}\overline{\chi_6^{(0)2}} - \chi_1^{(0)\prime}\chi_2^{(0)\prime}\overline{\chi_5^{(0)2}} - \overline{\chi_1^{(0)\prime}}\overline{\chi_2^{(0)\prime}}\chi_5^{(0)2} \\ & + 2\chi_1^{(0)\prime}\chi_3^{(0)}\overline{\chi_5^{(0)}}\chi_6^{(0)} + 2\overline{\chi_1^{(0)\prime}}\chi_3^{(0)}\chi_5^{(0)}\overline{\chi_6^{(0)}} \\ & + 2\chi_2^{(0)\prime}\chi_4^{(0)}\overline{\chi_5^{(0)}}\overline{\chi_6^{(0)}} + 2\overline{\chi_2^{(0)\prime}}\chi_4^{(0)}\chi_5^{(0)}\chi_6^{(0)} - 2\chi_3^{(0)}\chi_4^{(0)} \\ & \times(\chi_5^{(0)}\overline{\chi_5^{(0)}} + \chi_6^{(0)}\overline{\chi_6^{(0)}}) + (\chi_5^{(0)}\overline{\chi_5^{(0)}} - \chi_6^{(0)}\overline{\chi_6^{(0)}})^2, \end{aligned} \tag{A7}$$

$$\begin{aligned} N_\pm^a = {} & -\overline{\chi_1^{(0)\prime}}(\chi_2^{(0)\prime}\overline{\chi_2^{(0)\prime}} + \chi_3^{(0)2}) \pm \overline{\chi_1^{(0)\prime}}\chi_2^{(0)\prime}\overline{\chi_6^{(0)}} \\ & \mp \overline{\chi_1^{(0)\prime}}\chi_3^{(0)}\chi_5^{(0)} + \overline{\chi_2^{(0)\prime}}\chi_6^{(0)2} + \chi_2^{(0)\prime}\overline{\chi_5^{(0)2}} \\ & - 2\chi_3^{(0)}\overline{\chi_5^{(0)}}\chi_6^{(0)} \mp \chi_2^{(0)\prime}\chi_4^{(0)}\overline{\chi_5^{(0)}} \pm \chi_3^{(0)}\chi_4^{(0)}\chi_6^{(0)} \\ & \mp \chi_6^{(0)}\overline{\chi_6^{(0)2}} \pm \chi_5^{(0)}\overline{\chi_5^{(0)}}\chi_6^{(0)}, \end{aligned} \tag{A8a}$$

$$\begin{aligned} N_\pm^b = {} & -\chi_2^{(0)\prime}(\chi_1^{(0)\prime}\overline{\chi_1^{(0)\prime}} + \chi_4^{(0)2}) \pm \overline{\chi_1^{(0)\prime}}\chi_2^{(0)\prime}\overline{\chi_6^{(0)}} \\ & \mp \chi_2^{(0)\prime}\chi_4^{(0)}\overline{\chi_5^{(0)}} + \chi_1^{(0)\prime}\chi_6^{(0)2} + \overline{\chi_1^{(0)\prime}}\chi_5^{(0)2} \\ & - 2\chi_4^{(0)}\chi_5^{(0)}\chi_6^{(0)} \mp \overline{\chi_1^{(0)\prime}}\chi_3^{(0)}\chi_5^{(0)} \pm \chi_3^{(0)}\chi_4^{(0)}\chi_6^{(0)} \\ & \mp \chi_6^{(0)}\overline{\chi_6^{(0)2}} \pm \chi_5^{(0)}\overline{\chi_5^{(0)}}\chi_6^{(0)}. \end{aligned} \tag{A8b}$$

Notice that the longitudinal and transverse susceptibilities differ only in the signs of $\chi_5^{(0)}$ and $\chi_6^{(0)}$. Since $\mathrm{Im}(1/U)=0$, the constant terms in Eqs. (A6) do not contribute to the cross sections.

*Current address.

[1] For comprehensive reviews of Cr alloys, see E. Fawcett, Rev. Mod. Phys. **60**, 209 (1988); E. Fawcett, H. L. Alberts, V. Yu. Galkin, D. R. Noakes, and J. V. Yakhmi, *ibid.* **66**, 26 (1994).

[2] K. Mikke and J. Jankowska, in *Proceedings of the Conference on Transition Metals*, Toronto, 1977, edited by M. J. G. Lee, J. M. Perez, and E. Fawcett, IGP Conf. Proc. No. 39 (Institute of Physics and Physical Society, London, 1978), p. 599; J. Phys. F **10**, L159 (1980).

[3] C. R. Fincher, G. Shirane, and S. A. Werner, Phys. Rev. Lett. **43**, 1441 (1979).

[4] C. R. Fincher, G. Shirane, and S. A. Werner, Phys. Rev. B **24**,

1312 (1981); S. A. Werner, G. Shirane, C. R. Fincher, and B. H. Grier, in *Neutron Scattering—1981*, edited by John Faber, Jr. (AIP, New York, 1982), p. 269; B. H. Grier, G. Shirane, and S. A. Werner, Phys. Rev. B **31**, 2892 (1985).

[5] S. K. Burke, W. G. Stirling, K. R. A. Ziebeck, and J. G. Booth, Phys. Rev. Lett. **51**, 494 (1983).

[6] J. E. Lorenzo, B. J. Sternlieb, G. Shirane, and S. A. Werner, Phys. Rev. Lett. **72**, 1762 (1994).

[7] Y. Endoh, T. Fukuda, K. Yamada, and M. Takeda, J. Phys. Soc. Jpn. **63**, 3572 (1994).

[8] T. Fukuda, Y. Endoh, K. Yamada, M. Takeda, S. Itoh, M. Arai, and T. Otomo (unpublished).

[9] H. Sato and K. Maki, Int. J. Magn. **4**, 163 (1973) ; **6**, 183 (1974).

[10] T. Wolfram and S. Elliatioglu, Phys. Rev. Lett. **44**, 1295 (1980).

[11] Y. Kurihara, J. Phys. Soc. Jpn. **51**, 2123 (1982).

[12] G. C. Psaltakis, Solid State Commun. **51**, 535 (1984).

[13] R. S. Fishman and S. H. Liu, preceding paper, Phys. Rev. B **54**, 7233 (1996).

[14] R. S. Fishman and S. H. Liu, Phys. Rev. B **48**, 3820 (1993).

[15] P. A. Fedders and P. C. Martin, Phys. Rev. **143**, 8245 (1966).

[16] C. Y. Young and J. B. Sokoloff, J. Phys. F **4**, 1304 (1974).

[17] Y. Tsunoda, M. Mori, N. Kunitomi, and J. Kanamori, Solid State Commun. **14**, 287 (1974); S. Ida, M. Kohno, Y. Tsunoda, and N. Kunitomi, J. Phys. Soc. Jpn. **50**, 2581 (1981).

[18] S. Ida, Y. Tsunoda, Y. Nakai, and N. Kunitomi, J. Phys. Soc. Jpn. **50**, 2587 (1981).

[19] R. S. Fishman and S. H. Liu, Phys. Rev. Lett. **76**, 2398 (1996).

[20] R. S. Fishman and S. H. Liu, Phys. Rev. B **47**, 11 870 (1993); J. Phys. C **5**, 3959 (1993).

[21] E. Fawcett, S. A. Werner, A. Goldman, and G. Shirane, Phys. Rev. Lett. **61**, 558 (1988).

[22] D. R. Noakes, T. M. Holden, E. Fawcett, and P. C. deCamargo, Phys. Rev. Lett. **65**, 369 (1990).

[23] S. K. Sinha, S. H. Liu, L. D. Muhlestein, and N. Wakabayashi, Phys. Rev. Lett. **23**, 311 (1969); S. K. Sinha, G. R. Kline, C. Stassis, N. Chesser, and N. Wakabayashi, Phys. Rev. B **15**, 1415 (1977).

[24] J. Als-Nielsen, J. D. Axe, and G. Shirane, J. Appl. Phys. **42**, 1666 (1971).

[25] A. B. Harris, D. Kumar, B. I. Halperin, and P. C. Hohenberg, Phys. Rev. B **3**, 961 (1971).

[26] J. B. Sokoloff, Phys. Rev. **185**, 770 (1969); **185**, 783 (1969).

[27] P. A. Lee, T. M. Rice, and P. W. Anderson, Solid State Commun. **14**, 7031 (1974).

[28] A. W. Overhauser, Phys. Rev. B **3**, 3173 (1971).

[29] D. Jérome and H. Schulz, Adv. Phys. **31**, 299 (1981).

[30] Yu. A. Izyumov and V. M. Laptev, Zh. Eskp. Teor. Fiz. **88**, 165 (1985) [Sov. Phys. JETP **61**, 95 (1985)].

[31] T. Ziman and P. Lindgård, Phys. Rev. B **33**, 1976 (1986).

[32] X. Zhu and M. B. Walker, Phys. Rev. B **34**, 8064 (1986).

[33] A. Shibatani, K. Motizuki, and T. Nagamiya, Phys. Rev. **177**, 984 (1969).

[34] R. S. Fishman and S. H. Liu, Phys. Rev. B **49**, 3308 (1994), and references therein.